Post-weaning parvalbumin expression in left orbitofrontal cortex shapes sociability in female mice

Authors: Yi-Seon Jeon[1†], Daun Jeong[1†], Hanseul Kweon[1,2], Jae-Hyun Kim[1], Choong Yeon Kim[3], Youngbin Oh[1], Young-Ho Lee[1], Chan Hyuk Kim[1], Sang-Gyu Kim[1], Jae-Woong Jeong[3], Eunjoon Kim[1,2], and Seung-Hee Lee[1,*]

Affiliations:

[1]Department of Biological Sciences, KAIST, 291 Daehak-ro, Yuseong-gu, Daejeon, 34141, Korea

[2]Center for Synaptic Brain Dysfunctions, Institute for Basic Science, KAIST, 291 Daehak-ro, Yuseong-gu, Daejeon, 34141, Korea

[3]School of Electrical Engineering, Korea Advanced Institute of Science and Technology, Daejeon, Republic of Korea.

[†]These authors contributed equally to this work.

*Correspondence: shlee1@kaist.ac.kr (S.-H. L.)

Abstract

The adolescent social experience is essential for the maturation of the prefrontal cortex (PFC) in mammalian species. However, it is still unclear which cortical circuits mature with such experience and how it shapes adult social behaviors in a sex-specific manner. Here, we found that the post-weaning social isolation during adolescence (PWSI) caused hypersociability in female mice only and impaired both the parvalbumin (PV) expression and social sniffing-induced activity in the left orbitofrontal cortex (OFC_L). Similarly, the CRISPR/Cas9-mediated knock-down of PV in the OFC_L enhanced sociability and reduced the social sniffing-induced activity in female mice via decreased excitability of PV^+ neurons and reduced synaptic inhibition in the OFC_L. Moreover, optogenetic activation of OFC_L excitatory neurons enhanced sociability in female mice. Our data demonstrate that the adolescent social experience is critical for the maturation of PV^+ inhibitory circuits in the OFC_L; this maturation shapes female social behavior via enhancing social representation in the OFC_L.

Keywords: CRISPR/Cas9 / hypersociability / orbitofrontal cortex / parvalbumin / post-weaning social isolation

Introduction

One of the hallmarks of postnatal maturation in the mammalian cortex is the maturation of GABAergic inhibitory circuits (Luhmann & Prince, 1991). Maturation is accompanied by an increase in the expression of both the parvalbumin (PV) in a subset of GABAergic neurons and the perineuronal nets (PNNs) surrounding the PV^+ neurons (Celio & Blumcke, 1994; Huang *et al*, 1999). PV is a calcium-binding protein and a well-known genetic marker for fast-spiking GABAergic neurons in the cortex (Rudy *et al*, 2011). PV gene expression is upregulated in the sensory cortex in an activity-dependent manner (Krishnan *et al*, 2017; Sugiyama *et al*, 2008) after mammals are born. Like PV, PNNs also increase during cortical maturation and, in the adult cortex, surround most of the PV^+ neurons (Ueno *et al*, 2017; Ueno *et al*, 2018). Along with the increase of PNNs in cortical circuits, other molecular changes reduce net plasticity and facilitate the maturation of the cortical network (Beurdeley *et al*, 2012). If mice are deprived of visual input during the critical period after eye-opening, via monocular deprivation or dark rearing, PV^+ neurons are less developed, and PNNs are reduced in the primary visual cortex (V1) (Sugiyama *et al.*, 2008). This deprivation, in turn, diminishes both the visual response of V1 neurons that receive input from the deprived eye (Sugiyama *et al.*, 2008) and inhibition in the cortex (Dityatev *et al*, 2007). Therefore, the postnatal sensory experience is critical for the expression of PV and PNNs in PV^+ neurons, as these are required for the maturation of PV^+ inhibitory circuits and, eventually, for shaping sensory responses in the cortex (Hensch, 2005).

The maturation of the cortex occurs first in the sensory area, where the process is part of sensory experience, and later in the motor-frontal and the PFC (Hensch, 2005). Social experience is critical for the maturation of the PFC in both humans (Blakemore, 2008; Paus *et al*, 2008) and rodents (Makinodan *et al*, 2012) particularly during juvenile and adolescent periods. Patients with

57 autism or schizophrenia often show abnormal social cognition as well as dysfunction in the PFC
58 (Bicks *et al*, 2015). In these patients, the expression of PV and PNNs is reduced in the dorsolateral
59 PFC (Enwright *et al*, 2016; Wohr *et al*, 2015). Thus, it is plausible that immature PV^+ circuits in
60 the PFC cause the psychiatric symptoms underlying abnormal social behavior in mammals.
61 However, we still do not understand whether the social experience is required for PV^+ inhibitory
62 circuits in these PFC regions to mature. In particular, it is largely unknown whether the social
63 experience affects the maturation of inhibitory circuits in the orbitofrontal cortex (OFC), one of
64 the PFC sub-regions critical for social cognition (Adolphs, 2003; Amodio & Frith, 2006).

65 Mammalian social behavior is sexually dimorphic and important for maintaining a
66 conspecific society. Social behavior begins to become more sex-specific during adolescence.
67 Interestingly, how social information is processed and social behavior executed in the mammalian
68 brain shows hemispheric asymmetry and lateralization (Marlin *et al*, 2015). Even in rodents,
69 according to recent studies, the PFC functions asymmetrically in mediating social behaviors (Lee
70 *et al*, 2015). However, whether such asymmetry in the PFC becomes increasingly pronounced in
71 a sex-specific manner in response to social experience during adolescence is still unclear. In this
72 study, we investigated whether social experience influences the maturation of PV^+ neurons in the
73 PFC of each sex and in both hemispheres. We found that, in female mice, social experience during
74 adolescence is required for the maturation of PV^+ neurons in the left OFC (OFC_L) and for shaping
75 sociability. Using post-weaning social isolation (PWSI) and the CRISPR/Cas9 system, we
76 revealed that social isolation during adolescence caused the defect in PV expression in the OFC_L
77 of female mice, which led to hypersociability and reduced OFC_L activity during social contact.

Results

Post-weaning social isolation enhances sociability in female mice

Previous reports have shown that both short- and long-term social isolation affects mouse social behaviors (Makinodan *et al.*, 2012; Matthews *et al*, 2016). However, the effects differ depending on the duration of isolation, and the data were collected only in male mice. To examine whether the effects of short- and long-term social isolation on the mouse sociability differ between the sexes, we performed the sociability test in both male and female mice. For the sociability test, we put two small chambers at diagonal corners in the maze, each of which contained a novel object (O) or a novel and sex-matched mouse (M), and measured relative times of mice sniffing or spending at or nearby the novel mouse compared to those times at the novel object as indices of the mouse sociability. We quantified the sociability in mice that had experienced three different post-weaning social conditions at postnatal day 80 (P80): group-housed (GH), socially isolated for 1-day (1dSI), or socially isolated for 60-days after weaning (post-weaning social isolation, PWSI) (Fig 1A and B). Both the sniffing time of 1dSI mice when they came into contact with a novel mouse and their time spent in the social interaction zone did not differ significantly from those of GH mice in both males and females (Fig 1C and D).

Notably, PWSI induced changes in sociability in a sex-specific manner: only female mice showed a significant increase in social sniffing time and social interaction time, while PWSI male mice showed normal sociability as the GH mice (Fig 1C and D). We also confirmed that the effect of PWSI on female mice was not simply due to hormonal changes that occur during the estrous cycle. First, we confirmed that the estrous cycle was not different between GH and PWSI female mice (Fig 1E). We next confirmed that the mouse sociability (both social sniffing index and social interaction index) that we measured was consistent across the estrous cycle in female mice (Fig

101 1F-1H). Therefore, our data indicate that long-term social isolation during adolescence affects
102 social behavior in females more than in males, causing hypersociability in females.
103

104 **PWSI reduces PV expression in the OFC_L of female mice**

105 We next examined whether the social experience during adolescence is required for the
106 maturation of PV^+ inhibitory circuits in the OFC. We quantified the number of PV^+ or PNN^+
107 neurons in the OFC of the GH and the PWSI mice at P80. We collected data from male and female
108 mice separately. We first immunostained both for the PV, a marker for fast-spiking GABAergic
109 neurons, and the NeuN, a marker for all neurons (Fig 2A). We counted the number of
110 immunostained neurons automatically in the three coronal sections that were collected across the
111 center of the OFC (+2.1 ~ +2.34 mm from the bregma) per each hemisphere in each mouse (See
112 Methods; Fig 2B and C). Interestingly, the number of PV^+ and $NeuN^+$ neurons in the OFC was
113 significantly lower in the brains of PWSI female mice compared to the GH female mice, especially
114 in the left hemisphere (Fig 2D-G). In male mice, however, the number of PV^+ and $NeuN^+$ neurons
115 was not significantly different between GH and PWSI groups (Fig 2D-G). We next quantified the
116 PNN^+ neurons in the OFC by staining for *Wisteria floribunda agglutinin* (WFA), a marker for
117 PNNs (EV1A). There were both PV^+ and PV^- neurons surrounded by the PNNs in the OFC (Fig
118 S1B). We found that the numbers of WFA^+ neurons in the OFC were not different between GH
119 and PWSI in both male and female mice (Fig S1B and C). Collectively, our data indicate that
120 social experience during adolescence is crucial for the maturation of PV^+ neurons, especially the
121 PV expression, in the OFC_L of female mice.

122 PWSI mice experienced long-term social isolation from the time when they were weaned
123 at P21 to the time when they became adults at P80. This period includes both early juvenile periods

124 before the onset of puberty and late adolescence after the onset of puberty. Since puberty leads to
125 sexual dimorphism, we wondered whether the social experience after the onset of puberty is more
126 important for the female-specific maturation of the OFC. We thus re-group-housed the isolated
127 female mice at P50 and re-introduced them to social experience during late adolescence after the
128 onset of puberty. We then measured the social behaviors and the number of PV^+ neurons in the
129 OFC_L of the re-group-housed female mice at P80 (re-GH; Fig 3A). Not like the PWSI mice, which
130 showed an increase in sociability and a decrease of PV^+ neurons in the OFC_L, re-GH mice did not
131 show such changes compared to the GH mice (Fig 3B-D). These data indicate that social
132 experience during late adolescence from P50 to P80 is important for the PV^+ expression in the
133 OFC_L and maturation of normal social behaviors in female mice.
134

135 **PWSI disrupts social sniffing-induced activity in the OFC_L of female mice**

136 Because PV^+ neurons in the OFC_L were found to be less numbered following PWSI in
137 female mice, we investigated whether the OFC_L neural response to social contact has been altered
138 in head-fixed female mice by *in vivo* multichannel recordings (Fig 4A). During the recording, both
139 GH and PWSI female mice showed both object-sniffing and social sniffing behavior under the
140 head-fixed condition, and the number and duration of sniffing times did not differ between groups
141 (Fig S2A-C). We identified neurons that showed significant sniffing-induced activity in the OFC
142 (Fig 4B-D). Interestingly, in GH females, more neurons showed sniffing-induced activity in the
143 OFC_L than in the OFC_R responses, and their responses were stronger when a mouse sniffed another
144 mouse than when it sniffed an object (Fig 4C-F). More important, social sniffing-induced activity
145 in the OFC_L of female mice disappeared after PWSI (Fig 4C, E and F). On the other hand, the
146 sniffing-induced activity of the OFC_R did not differ between GH and PWSI female mice (Fig 4D).

147 These data indicate that PWSI disrupted social sniffing-induced neural activity and reduced social
148 representation in the OFC_L.

149

150 **PV^+ expression, not PNNs in the OFC_L, shapes social behavior in female mice**

151 As we found that PWSI impaired the PV expression in the OFC_L and increased social
152 behavior, we next examined the causal relationship between the reduction of PV expression in the
153 OFC_L and the increase in the sociability of female mice. To test this, we used the CRISPR/Cas9
154 system (Swiech *et al*, 2015) to remove the PV gene selectively in the nucleus and thus induce
155 overall knock-down of PV expression in the OFC_L. We designed two pairs of single-guide RNAs
156 (sgRNAs) to target the 4th and 5th exons of the PV gene (sgPV) and confirmed that those sgRNAs
157 knocked out the PV gene by either deletion or insertion of the targeted sequences in more than 85%
158 of the Cas9-transfected Neuro2a cells (Fig S3A-D). We then constructed the adeno-associated
159 viral vectors (AAVs) to deliver the sgRNAs together with the tdTomato gene to neurons *in vivo*
160 (Fig 5A; S3A). To knock out the PV gene in the PV^+ interneurons *in vivo*, we injected the AAVs
161 into the cortex of mice crossed between PV-Cre and $Cas9^{fl/fl}$-eGFP mice (sgPV; and Fig 5A; Fig
162 S3E-G). In these sgPV mice, the neurons that express both eGFP and tdTomato were originally
163 the PV^+ neurons, but their PV gene was knocked out by Cas9 (Fig 5A). As a control, we injected
164 the AAV that expressed only the tdTomato without sgRNAs to the crossed mice (tdTom). We first
165 immunostained the PV and the PNNs in the injected brain samples and confirmed that the
166 $eGFP^+$/$tdTomato^+$ neurons were selectively knocked down with PV, without any decrease of PNN
167 expression (Fig 5B). We next performed the sociability test on the female mice that had been
168 knocked down with PV in the OFC_L. These mice showed a significant increase in sociability (Fig
169 5C and D), similar to the PWSI females (Fig 1B-D).

170 We further examined whether the PNN expression surrounding PV^+ neurons are also
171 altered by the PWSI and influences the female sociability. We infused chondroitinase ABC
172 (chABC), an enzyme that degrades PNNs by removing sulfate side chains of proteoglycans, into
173 the OFC_L (Fig 5E). Treatment with chABC removed PNNs surrounding PV^+ neurons without
174 affecting PV expression (Fig 5F, left) and significantly decreased the number of WFA^+ neurons in
175 the OFC_L (Fig 5F, right). We then performed the sociability test on the female mice treated with
176 chABC and found that they showed normal sociability (Fig 5G and H). Together, our data indicate
177 that the PV expression, but not the PNN maturation, in the OFC_L was a key factor shaping social
178 behavior of female mice.

179

180 **Decrease in PV expression reduces social sniffing-induced activity via hyper-excitation of**
181 **OFC_L neurons**

182 We next investigated whether the decrease of PV expression in the OFC_L was responsible
183 for the reduced sniffing-induced activity in the OFC_L of the PWSI female mice. We performed *in*
184 *vivo* recordings in female mice injected with sgPV AAVs (**sgPV**) or injected with tdTomato AAVs
185 (**tdTom**) in their OFC_L (Fig 6A-G). First, we found that the average baseline firing rates were
186 significantly higher in the spPV group compared to the tdTom group (Fig 6D and E). Furthermore,
187 similar to PWSI, knocking down PV by sgPV decreased social sniffing-induced activity in the
188 OFC_L of female mice (**sgPV**; Fig 6F and G). Conversely, the expression of tdTomato in the OFC_L
189 did not alter the sniffing-induced activity of female mice (**tdTom**; Fig 6F and G). Knocking down
190 PV in the OFC_L did not affect the sniffing behavior itself, as the number and duration of sniffs in
191 the altered mice were similar to those in the tdTom control mice (Fig S1D and E). These data

192 indicate that the knock-down of PV increased overall firing activity while reducing the sniffing-
193 induced activity in the OFC_L.

194 As we observed an increase in the baseline activity of OFC_L neurons by knocking down
195 the PV, we next examined whether the knock-down of PV has altered the excitation-inhibition
196 balance in the OFC_L of female mice. We first performed patch-clamp recordings of the PV^+
197 neurons in the OFC_L by targeting $tdTomato^+$ neurons of PV::Cas9 mice injected with sgPV or
198 tdTom AAVs into the OFC_L (Fig 6H-L). We found that the knock-out of the PV gene by sgPV in
199 PV^+ neurons reduced the intrinsic excitability of those neurons (Fig 6I) without any changes in
200 spontaneous excitatory synaptic currents (sEPSCs; Fig 6L). Other membrane properties, such as
201 the half-width of spike waveforms and the input resistance, were normal in those neurons (Fig 6J
202 and K). We next measured the spontaneous inhibitory postsynaptic currents (sIPSCs) in the OFC_L
203 neurons, which were not labeled with the tdTomato in the sgPV and the tdTom mice. These
204 neurons were regular spiking and thus putative excitatory neurons in the OFC_L (Fig 6H and M).
205 The OFC_L excitatory neurons in the sgPV mice showed a significant decrease in both amplitudes
206 and frequencies of spontaneous IPSCs compared to the tdTom control mice (Fig 6M). These data
207 indicate that the decreased expression of PV in the OFC_L reduced the excitability of the PV^+
208 neurons and, in turn, reduced inhibition of the neighboring neurons in the OFC_L of female mice.

209 Our recording data suggested that the decrease in inhibition upon knocking down the PV
210 gene caused an increase of excitation, which led to a rise in the baseline activity of OFC_L and
211 disruption in sniffing-induced activities (Fig 6D-G). We thus examined whether the abnormal
212 increase of the OFC_L activity caused hypersociability in female mice. We expressed the
213 channelrhodopsin-2 (ChR2) in the excitatory neurons of the OFC_L by injecting the AAV virus,
214 which expresses the ChR2 fused to the eYFP under the CaMKIIα promotor, to the wild-type

215 female mice (Fig 7A). We then delivered the light stimulation to the OFC_L by inserting a wireless
216 optogenetic device that we developed (Kim *et al*, 2021; Qazi *et al*, 2021) to provide the 20Hz blue
217 lights during the sociability tests (Fig 7B; see Methods). The stimulation was given on the second
218 day of the sociability tests. We measured the first-day sociability (Day1) without the light
219 stimulation and did not observe any differences in the sociability between the ChR2-eYFP and the
220 eYFP groups. On the second day, we tested their sociability again but with the blue-light
221 stimulation on the OFC_L (Day2). The eYFP control mice showed a significant decrease in their
222 sociability on Day2 compared to Day1 potentially due to habituation (Fig 7C and D). On the other
223 hand, the ChR2-eYFP-expressed mice showed higher levels of social sniffing behaviors than the
224 control mice (Fig 7C), showing no such habituation on Day2 compared to Day1 (Fig 7D).
225 Therefore, the optogenetic activation of the OFC_L resulted in less habituation in their social
226 behavior and induced higher sociability on Day2 (Fig 7D). The light stimulation did not affect the
227 locomotion in both groups (Fig 7E). Collectively, our data demonstrate that the reduced expression
228 of the PV caused hyper-excitation of the OFC_L, which led to hypersociability in female mice.
229

230 **Discussion**

231 In this study, we found that social experience during adolescence is critical for shaping
232 sociability in female mice. PWSI enhanced sociability in female mice while impairing the
233 maturation of PV^+ neurons and decreasing social sniffing-induced activity in the OFC_L. The
234 knock-down of PV in the OFC_L of female mice induced the same phenotype as the PWSI mice:
235 enhanced sociability and decreased sniffing-induced activity in the OFC_L. These effects were due
236 to the imbalance between excitation and inhibition, as the PV knock-down caused an increase in
237 excitation in the OFC_L. We further found that optogenetic activation of the OFC_L led to enhanced

238 sociability in female mice. Our data indicate that adolescent social experience is critical for
239 balancing excitation with inhibition via maturation of PV^+ inhibitory circuits in the OFCL to shape
240 sociability in female mice. Our data also suggest that adolescent social experience functions
241 differently in male and female mice, both in how the prefrontal cortex matures and how social
242 behavior matures.

243

244 **Importance of social experience during adolescence in shaping female social behavior**

245 Social experience during adolescence is important for the maturation of the mammalian
246 brain (Fuhrmann *et al*, 2015; Makinodan *et al.*, 2012). In humans, mistreatment or the lack of
247 social care at a young age can increase the occurrence of neurological disorders and cause defects
248 in brain function (Egeland *et al*, 1983; Hanson *et al*, 2010; Widom *et al*, 2007). Similarly,
249 depriving rodents of social experience during adolescence caused defects in the maturation of their
250 brains and behavior (Cooke *et al*, 2000; Schubert *et al*, 2009), and some of the physiological effects
251 of social isolation were sex-specific (McCormick *et al*, 2008; Pisu *et al*, 2016). We used PWSI to
252 deprive mice of social experiences during adolescence. Our data showed that female mice are more
253 vulnerable to social isolation during late adolescence after the onset of puberty than male mice.

254 A recent study has shown that the 1dSI increased sociability in male mice (Matthews *et al.*,
255 2016). We also found male mice that had experienced 1dSI spent more time interacting with a
256 novel mouse than did GH male mice (GH, 221.11 ± 17.93 s, 1dSI, 317.97 ± 31.46 s, p=0.023,
257 student's t-test), but they also showed a tendency of increased interaction with an object (GH,
258 107.29± 9.88 s, 1dSI, 138.28 ± 23.36 s, p=0.256, student's t-test). Therefore, the social sniffing
259 and social interaction indices, which indicate the ratio between social interaction and object
260 interaction times, were comparable between GH and 1dSI male mice (Fig 1C and D). In female

261 mice, 1dSI had no specific effects on social and object interaction times. Collectively, our data
262 demonstrate that long-term social isolation during adolescence affects social behaviors more
263 strongly than the 1dSI specifically in females.

264 PWSI causes sensory deprivation because mice are prevented from interacting socially
265 with other mice. Furthermore, PWSI causes stress in social mammals (Fone & Porkess, 2008), and
266 social isolation lasting more than 1 day has been used to induce chronic stress in rodents (Fone &
267 Porkess, 2008). It has been shown that both sensory deprivation and stress can impair the
268 maturation of PV^+ neurons in the sensory cortex as well as in the hippocampus (Czeh *et al*, 2005;
269 Hu *et al*, 2010; Huang *et al.*, 1999). The OFC, which is classified as a secondary olfactory cortex,
270 is one of the key areas involved in olfactory processing (Lipton *et al*, 1999) as well as in sniffing
271 behavior (Kareken *et al*, 2004). Furthermore, the olfactory system is the most important way
272 through which mice detect other mice (Radyushkin *et al*, 2009). The OFC has a strong connection
273 with both the olfactory system and the hippocampus (Wikenheiser & Schoenbaum, 2016). Thus,
274 it is possible that the olfactory deprivation and the stress that characterizes PWSI caused the
275 decrease in PV expression in the OFC_L. Future studies are necessary to unravel which types of
276 social olfactory cues and stress-related factors affect the maturation of PV^+ neurons in the OFC_L
277 and social behavior.

278 Our findings demonstrate that the OFC_L plays a key role in shaping social behavior, especially
279 in female mice. Supporting this idea, an fMRI study in humans showed that in response to odorant
280 cues with emotional valence, only females showed increased activity in their OFC_L (Royet *et al*,
281 2003). Thus, the female OFC_L seems to have evolved to recognize the valence of odorant cues,
282 namely, those that characterize social cues in mammals. Our data further suggest that social
283 experience shapes this function of the OFC_L during adolescence, particularly after the onset of

284 puberty, in females. Moreover, we found that PWSI caused a decrease in the activity of the OFC_L
285 while enhancing sociability. Excessive sociability is a symptom of patients with Williams
286 syndrome, a rare neurodevelopmental genetic disorder that shows abnormal activity patterns in the
287 OFC (Mimura *et al*, 2010). Our data further demonstrate that PWSI induced hypersociability,
288 which is similar to Williams syndrome, in female mice and that the normal maturation and activity
289 of the OFC_L is important for maintaining an adequate level of sociability in females.
290

291 **PV expression in the OFC is important for social behavior**

292 The maturation of PV^+ inhibitory circuits occurs by increasing the expression of PV and
293 PNNs, balancing inhibition with excitation in the cortex; this balance is critical for shaping sensory
294 responses (Hensch, 2004). Recent studies have examined the correlation between cognitive
295 behaviors and PV expression in the PFC. For example, several mouse models of autism that show
296 decreased sociability have shown reduced PV expression in the mPFC (Kobayashi *et al*, 2018) as
297 well as in the striatum (Filice *et al*, 2016). Furthermore, early-life stress occasioned by maternal
298 separation before weaning reduced PV expression in the OFC of female mice and impaired their
299 flexibility (Goodwill *et al*, 2018). Interestingly, the reduced expression of PV in the dorsolateral
300 PFC was observed in human patients with schizophrenia (Enwright *et al.*, 2016; Nakazawa *et al*,
301 2012) and autism (Ferguson & Gao, 2018). However, none of these studies proved that PV
302 expression in the PFC caused the deficits that characterize those cognitive behaviors. Although the
303 whole-brain knock-out of PV caused the mice to show autism-like behavior (Wohr *et al.*, 2015),
304 we still do not know the specific function of the PV in sub-regions of the PFC. Our study used the
305 CRISPR/Cas9 system to knock down the PV expression locally in the OFC_L. This method found
306 that PV expression in the OFC_L is critical for shaping mouse social behavior (Fig 5).

307 PV is a calcium-binding protein that plays a key role in regulating the physiological
308 properties of PV^+ neurons. Electrophysiological studies have revealed that knocking down PV in
309 fast-spiking interneurons in the striatum enhanced the fast-spiking properties of those neurons and
310 increased the paired-pulse ratio of the inhibitory release to postsynaptic neurons (Orduz *et al*,
311 2013) while decreasing the paired-pulse ratio of evoked excitatory inputs to those neurons (Wohr
312 *et al.*, 2015). We further found that knocking down PV decreased the excitability of the inhibitory
313 neurons, which in turn decreased synaptic inhibition on nearby excitatory neurons (Fig 6H-M).
314 The reduced inhibition in the OFC_L, which was induced either by the knock-out of PV or by the
315 optogenetic activation of excitatory neurons in the OFC_L, caused hypersociability potentially due
316 to the disruption of overall social sniffing-induced activity in the OFC_L (Fig 6F and G). Moreover,
317 reduced PV expression can also disrupt the network property of the OFC_L, similar to the previous
318 report showing that the reduction of PV expression correlates with a decrease in the network
319 oscillation in the PFC (Lodge *et al*, 2009). Maturation of network activity during adolescence may
320 be critical for shaping social sniffing-induced activity in the OFC_L.

321 In a study of virgin female mice, PV and PNN expression in the auditory cortex was reported
322 to be correlated with learning to retrieve pups (Krishnan *et al.*, 2017); this activity, which occurs
323 in the left auditory cortex, is important for shaping maternal behaviors in female mice (Marlin *et*
324 *al.*, 2015). Our data further support the idea that plasticity in PV^+ neurons in the OFC_L is important
325 for shaping female sociability and is also characterized by hemispheric asymmetry. Both genetic
326 and epigenetic mechanisms have been identified as critical for regulating normal social behavior
327 (Hensch, 2005), and thus social behaviors can be easily disrupted in a wide range of brain
328 psychiatric disorders (Blakemore, 2008). Our study provides insight into how epigenetic

329 mechanisms, such as PV expression in the PFC, may underlie abnormal hypersociability that
330 characterizes certain psychiatric disorders.

Materials and Methods

Experimental model and subject details

We approved all experimental procedures from the KAIST Institutional Animal Care and Use Committee (IACUC-18-236). We maintained all mice ad libitum under light from 8 am to 8 pm and dark cycle from 8 pm to 8 am. All mice were weaned at postnatal day 21 (P21); mice were reared in double (28cm × 17cm × 14cm) cages with 3-5 mates for group housing or in single (20cm × 10cm × 14cm) cages alone for social isolation. We performed experiments on WT (C57BL/6J), PV-Cre (JAX, #008069), and the Rosa26-floxed STOP-Cas9 knock-in (JAX # 024857) mice.

Histology

We anesthetized mice with isoflurane and then perfused them with 1X phosphate-buffered saline (PBS) and 4% paraformaldehyde (PFA, w/v in PBS). Mouse brain samples were post-fixed for 4h at 4℃; after fixation, we incubated them in 30% sucrose solution (w/v in PBS) for 1-2 days at 4℃. Then, we embedded each brain sample in optimal cutting temperature medium (OCT, Tissue-Tek, Cat#4583) and froze each at -80℃. We sectioned frozen brains using a cryostat (Leica) and collected coronal sections either at 30 μm (for confirming injection sites) or 15 μm (for immunostaining) thickness. For confirming injection sites, brain sections were washed three times with 1X PBS and mounted in DAPI-containing mounting medium (VECTASHIELD®, cat#H-1200). For immunostaining, we washed the brain sections three times with 1X PBS and permeabilized them with 0.3% Triton X-100 in 1X PBS for 30 min. After the sections were incubated in a blocking solution (2% normal donkey serum in 1X PBS) for 2 hours at room temperature, we incubated them with primary antibodies (rabbit anti-PV, 1:500 dilution in

353 blocking solution, Swant, cat#PV25; mouse anti-NeuN, 1:500 dilution in blocking solution,
354 Millipore, cat#MAB377) for 2 days at 4℃. Last, we incubated them with fluorescence-tagged
355 secondary antibodies (Alexa Fluor 594 donkey anti-rabbit IgG for PV staining, 1:500 dilution in
356 1X PBS, Life Technology, cat#A21207; Alexa Fluor 647 donkey anti-mouse IgG for NeuN
357 staining, 1:500 dilution in 1X PBS, Jackson Immunoresearch, cat#715-605-151) and Fluorescein
358 (FITC) labeled Wisteria Floribunda Lectin (WFA, WFL) for PNN staining (1:500 dilution in 1X
359 PBS, Vector labs, cat#FL-1351) for 2 hours at RT before mounting them in clear mounting
360 medium (DAKO, cat#S3023). We imaged fluorescent signals of mounted brain sections under a
361 scanning microscope (ZEISS, Axio Scan.Z1).

362 **Cell counting analysis**

363 We matched the images obtained from the scanning microscope to the mouse brain atlas
364 (Franklin & Paxinos) to confirm the anterior-to-posterior location of the coronal brain sections.
365 We collected 15μm brain sections in every 60μm thickness across the frontal cortex, and we
366 selected three sections in a row that include OFC areas (between +2.10mm ~ +2.34mm anterior
367 from the bregma) for the immunostaining (see Fig 2C). We scanned the fluorescent images of the
368 brain sections and put a 0.3 x 0.3mm^2 square as a region-of-interest at the center of the OFC
369 (±1.3mm lateral from the bregma; depth, -2.5mm) to count the labeled neurons in the OFC. To
370 quantify the number of PV$^+$ and NeuN$^+$ neurons, we used the automatic cell counting software
371 (ImageJ). After converting the fluorescent images to the 8-bit grayscale images, we further
372 transformed the grayscale images into binary images. For the binary transition, we used distinct
373 thresholds at the grayscale for isolating the NeuN$^+$ neurons (11% of total mean intensity) and the
374 PV$^+$ neurons (2% of total mean intensity). We then automatically counted the white-filled circles
375 as cells if they satisfied the following conditions: 1) total size is above 60 x 60 pixels and 2) the

376 circularity is above 0.2. There was no significant difference between the number of cells counted
377 automatically and the number of cells counted manually in a blind manner (see Fig 2B). To validate
378 the knock-down efficiency of sgPV or chABC (see Fig 5), we manually and blindly counted the
379 number of PV^+ or WFA^+ neurons within 0.5 x 0.5mm^2 regions-of-interest in three representative
380 coronal sections covering OFC.

381 **Sociability test**

382 We performed the sociability test at either P79-81 or at P50. Before behavior experiments,
383 all mice were habituated 30-60 minutes in the habituation chamber. All mice were maintained in
384 a group-housed condition or an isolated condition until the habituation. Mice were then moved to
385 the sociability maze (50cm × 45cm × 20cm) where two containers were located diagonally at
386 opposite corners. The sociability test consisted of two phases: 1) habituation in the sociability maze
387 (empty containers, 10min) and 2) sociability test (an object container and a social container with
388 a young, same-sex, and stranger mouse, 10min). We used a software, EthoVision®XT 11.5
389 (Noldus), to analyze interaction times. We analyzed mouse sociability by two indicators: time
390 spent in interaction zones near the container (18cm × 18cm) and sniffing time. We calculated the
391 social sniffing and social interaction indices as follows:

392 $$\text{Social sniffing index} = \frac{(Social\ sniffing\ time)}{(Object\ sniffing\ time) + (Social\ sniffing\ time)}$$

393 $$\text{Social interaction index} = \frac{(Time\ in\ social\ zone)}{(Time\ in\ object\ zone) + (Time\ in\ social\ zone)}$$

394 **Measuring estrous cycle in female mice**

395 We monitored estrous cycle of female mice using vaginal cytology (McLean *et al*, 2012).
396 Vaginal smears from subject mice were collected right after the sociability test. Smears were
397 placed on slides and stained with 0.1% crystal violet (Sigma Aldrich, cat#V5265). Each estrous
398 cycle stage was determined based on the cell type that was mainly observed in the smear sample
399 among the three types: nucleated epithelial cells, cornified squamous epithelial cells, and
400 leukocytes. To examine the difference in estrous cycles between GH and PWSI, we performed the
401 vaginal cytology for four consecutive days in each mouse.

402 ***In vivo* extracellular recordings for measuring sniffing-induced activity**

403 We performed all recordings in the head-fixed and awake mice. We marked the top of left
404 and right OFCs and implanted custom-designed head-plates on the skull of mice using dental
405 cement and small screws. After 2-3 days of recovery, we habituated mice to be head-fixed for
406 20min per day for 3 days. After the habituation, we performed the recording in the OFC by making
407 a small craniotomy on the marked spots and inserting 32 channel silicon probes (A1X32-Poly2-
408 10mm-50-177 or A1X32-Poly3-10mm-50-177, Neuronexus) vertically into each OFC using a
409 micro-drive manipulator (Siskiyou). We first recorded spiking activity in the OFC without
410 presenting a stranger mouse for 10 min ($object_{sniffing}$ session) and next continuously recorded
411 neural activity while presenting a head-fixed stranger mouse in front of the recorded mouse for 10
412 min ($social_{sniffing}$ session). During the recording, we monitored and recorded the sniffing behavior
413 of the mouse by using a web camera (Microsoft, LifeCam HD-3000). All extracellular signals were
414 recorded at a 30kHz sampling rate, filtered between 500~5000Hz, and amplified by a miniature
415 digital headstage (CerePlex μ, Blackrock Microsystems). After the recording, we confirmed the
416 recording sites by injecting red retrobeads (Lumaflour) into the recording areas and performing
417 histology.

418 *Automatic quantification of sniffing behaviors*

419 We developed a Matlab code to automatically analyze sniffing events during object- and
420 social sniffing sessions in head-fixed mice. First, we converted all the RGB image frames of a
421 recorded video clip to a grayscale using the '*rgb2gray*' function. Next, we chose the region of
422 interest (ROI) including the nose and whiskers of the mouse being recorded, made a binary matrix
423 with 1 inside the ROI and 0 outside the ROI of each pixel, and multiplied an original image by the
424 binary matrix of each corresponding pixel along all the frames (ROI_1). We subtracted
425 background brightness from ROI_1 to eliminate overall brightness fluctuations (ROI_2), and
426 calculated deviations of brightness within the ROI by subtracting the mean brightness of each pixel
427 (ROI ΔF). To detect sniffing events, we subtracted a moving average (F_0, sliding window = 50
428 frames) from ROI ΔF (ROI $\Delta F–F_0$), and set a threshold by multiplying a median of absolute ROI
429 $\Delta F–F_0$ by 4. If ROI $\Delta F–F_0$ in each frame crossed the threshold, we included the frame in a sniffing
430 event.

431 *Neural activity analysis*

432 We performed the spike-sorting using Klusters software (http://neurosuite.sourceforge.net/)
433 (Hazan *et al*, 2006). We grouped 32-channel data into eight groups and sorted single units by
434 principal components analysis. We only isolated single units that show more than a 2 ms refractory
435 period in their auto-correlogram. We performed all other analyses using custom-made codes in
436 Matlab (Mathworks). We sorted sniffing trials in object sessions and social sessions by identifying
437 sniffing events across the recording sessions. We only used trials that satisfied the following two
438 criteria: 1) inter-sniffing interval (time between the offset of sniffing in current trial and the onset
439 time of the next trial) > 5sec, and 2) sniffing-duration (time between the onset and the offset of

440 sniffing in one trial) > 1sec. To plot the peri-event time histogram (PETH) of all neurons as a
441 population, we performed Z-scoring by averaging firing rates (Hz) of individual units across trials
442 and normalized them by 1sec baseline activity (3 to 2 sec before the onset of sniffing). The
443 normalized firing rates were convolved with a Gaussian filter (σ = 50ms) only for visualization
444 purposes. To identify the neurons showing significant sniffing-induced activity, we statistically
445 compared the firing rates of individual neurons during the 2 sec pre-period (3 to 1 sec before the
446 onset of sniffing) and 2 sec post-period (0 to 2 sec after the onset of sniffing) of each sniffing trial
447 by bootstrapping ($p < 0.01$, $n = 5000$). We quantified the sniffing-induced activity of neurons by
448 averaging Z values during 0 to 2 sec after the onset of sniffing. We classified cell types of recorded
449 neurons based on spike waveforms by quantifying spike widths of each isolated neuron (time
450 between peak and through of the spike, μs). If the spike width was below 350 μs or above 450 μs,
451 recorded neurons were classified as fast-spiking (FS) neurons or regular-spiking (RS) neurons,
452 respectively. For the baseline activity analysis, we quantified the average firing rates (Hz) from 0
453 to 2 sec before the onset of sniffing.

454 **Perineuronal net degradation**

455 To remove the PNN, we reconstituted protease-free chABC (Amsbio) in PBS to a final
456 concentration of 61U/ml. We injected female mice OFC_L with 0.5μl of PBS or chABC on postnatal
457 day 70-75. Seven days after the injection, we performed behavior experiments and sacrificed the
458 mice to confirm PNN degradation.

459 **CRISPR / Cas9 experiments**

460 *Generating of the PX552-sgPV-tdTomato*

To generate the AAV-tdTomato vector, we first replaced the eGFP gene in PX552 (Addgene # 60958) with tdTomato. The tdTomato template was obtained from pAAV-FLEX-tdTomato (Addgene # 28306). Next, we cloned two AAV-tdTomato plasmids, both of which induce the targeted mutations at the parvalbumin gene (sgPV). One virus expresses two sgRNAs targeting parvalbumin exon4: sgRNA1, 5'-AGACAAGTCTCTGGCATCTG-3' and sgRNA2, 5'-AAGGATGGGGACGGCAAGAT-3' (Cloned recombinant DNA fragment: AGACAAGTCTCTGGCATCTGGTTTTAGAGCTAGAAATAGCAAGTTAAAATAAGGCT AGTCCGTTATCAACTTGAAAAAGTGGCACCGAGTCGGTGCAACAAAGCACCAGTGG TCTAGTGGTAGAATAGTACCCTGCCACGGTACAGACCCGGGTTCGATTCCCGGCTGG TGCAAAGGATGGGGACGGCAAGATGTTTTAGAGCTAGAAATAGCAAGTTAAAATAA GGCTAGTCCGTTATCAACTTGAAAAAGTGGCACCGAGTCGGTGC, Bioneer & In-house PCR amplication), and the other virus expresses two sgRNAs targeting parvalbumin exon5: sgRNA3, 5'-GCTAAGTGGCGCTGACTGCT-3' and sgRNA4, 5'-GGCCGCGAGAAGGACTGAGA-3'(Cloned recombinant DNA fragment: GCTAAGTGGCGCTGACTGCTGTTTTAGAGCTAGAAATAGCAAGTTAAAATAAGGCT AGTCCGTTATCAACTTGAAAAAGTGGCACCGAGTCGGTGCAACAAAGCACCAGTGG TCTAGTGGTAGAATAGTACCCTGCCACGGTACAGACCCGGGTTCGATTCCCGGCTGG TGCAGGCCGCGAGAAGGACTGAGAGTTTTAGAGCTAGAAATAGCAAGTTAAAATAA GGCTAGTCCGTTATCAACTTGAAAAAGTGGCACCGAGTCGGTGC, Bioneer & In-house PCR amplication).

After cloning the AAV-tdTomato vectors, we transfected them with packaging plasmid into HEK293T (KCTC, cat# HC20005) to produce AAV-sgPV-tdTomato (exon4 and exon5) and AAV-tdTomato, using lipofectamine 2000 (Invitrogen, cat# 11668-019). After 72hr, we collected

484 AAV (AAV2) particles from the cell lysates and performed iodixanol gradient ultracentrifugation.
485 Next, we concentrated the viral particles with Amicon Ultra Centrifugal Filter (Millipore) and
486 quantified the concentration of viral particles by quantitative PCR (genome copies per ml; AAV-
487 tdTomato, 3.92×10^{14}; AAV-sgPV(exon4)-tdTomato, 3.07×10^{12}; AAV-sgPV(exon5)-tdTomato,
488 7.17×10^{12}).

489 *Validation of CRISPR/Cas9 in the Neuro2a cell*

490 To identify the efficiency of sgPV in knocking down the PV, we transfected cloned AAV
491 vectors with the Cas9-eGFP expressing vector (PX458) in the Neuro2a cells. After 72h, we
492 collected cells and sorted tdTomato/eGFP double-positive cells using BD FACSAria II (BD
493 Biosciences). Next, we purified genomic DNA from sorted cells and performed PCR to amplify
494 target sites of the PV gene, adding the index sequence for sequencing. Last, we subjected the
495 samples to Miniseq (Illumina) and analyzed insertion and deletion frequencies using CRISPR
496 RGEN Tools (http://www.rgenome.net/).

497 *Behavior and physiological experiments with CRISPR/Cas9 mice*

498 To express Cas9 selectively in PV^+ neurons, we crossed the PV-Cre mice (JAX #008069)
499 with the Rosa26-floxed STOP-Cas9 knock-in mice (JAX # 024857). We injected AAV-tdTomato
500 (tdTom) or AAV-sgPV-tdTomato (sgPV) to the crossed mice on the postnatal day 50-65. On
501 postnatal day 78-85, we performed the behavior test and *in vivo* recording. To verify whether the
502 AAV expression knocked down the PV effectively, we collected brain samples of the injected
503 mice and performed immunohistochemistry as described above. We used the combination of the
504 primary (rabbit anti-PV for PV staining, goat anti-GFP for Cas9 staining) and the secondary (Alexa
505 Fluor 405 donkey anti-goat IgG and Alexa Fluor 647 donkey anti-rabbit IgG were used) antibodies.

506 *Whole-cell patch-clamp recordings in brain slices*

507 For electrophysiology experiments, brain samples were collected from anesthetized mice
508 with isoflurane (Terrell) and sectioned (coronal, 300 μm thickness) using a vibratome (Leica
509 VT1200). Brain extraction and sectioning were conducted in ice-cold dissection buffer containing
510 (in mM) 212 sucrose, 25 $NaHCO_3$, 5 KCl, 1.25 NaH_2PO_4, 0.5 $CaCl_2$, 3.5 $MgSO_4$, 10 D-glucose,
511 1.25 L-ascorbic acid and 2 Na-pyruvate bubbled with 95% O_2/5% CO_2. The sectioned slices were
512 incubated in a recovery chamber at 32 °C with normal ACSF (in mM: 125 NaCl, 2.5 KCl, 1.25
513 NaH_2PO_4, 25 $NaHCO_3$, 10 glucose, 2.5 $CaCl_2$ and 1.3 $MgCl_2$, oxygenated with 95% O_2/5% CO_2).
514 After 60-min recovery at 32 °C, slices were incubated for 30 min at room temperature (20–25 °C).
515 Slice was transfered to a recording chamber at 27–29 °C with circulating ACSF saturated with
516 95% O_2 and 5% CO_2. Recording pipettes were made from thin-walled borosilicate capillaries (30–
517 0065, Harvard Apparatus) with resistance 3.0–4.0 MΩ using a two-step vertical puller (PC-10,
518 Narishege).

519 Whole-cell patch-clamp recordings were conducted using a MultiClamp 700B amplifier
520 (Molecular Devices) and Digidata 1550 (Molecular Devices). During the recordings,
521 hyperpolarizing step pulses (5mV, 40ms) were injected into the cell to monitored membrane
522 resistance calculated by peak amplitude of the capacitance current. Data from cells that changed
523 the resistance more than 20% were excluded. To measure the intrinsic excitability, recording
524 pipettes (3.0–4.0MΩ) were filled with an internal solution containing (in mM) 137 K-gluconate, 5
525 KCl, 10 HEPES, 0.2 EGTA, 10 Na-phosphocreatine, 4 Mg-ATP, and 0.5 Na-GTP, with pH 7.2,
526 280 mOsm. Picrotoxin (Sigma, 100μM), NBQX (Tocris, 10μM) and D-AP5 (Tocris, 50μM) were
527 added to ACSF to inhibit postsynaptic responses. After gigaseal and rupture, currents were
528 clamped, and RMP was maintained at -70mV. To measure the I-V curve, current inputs were

529 increased from -300 to 120pA in increments of 30pA per sweep with the time interval of 2 seconds.
530 To measure the I-F curve, current inputs were increased from 0 to 660pA in increments of 60pA
531 per sweep with the time interval of 10 seconds. For measuring sEPSCs in the OFC PV^+ neurons,
532 glass pipettes were filled with an internal solution composed of (in mM) 100 $CsMeSO_4$, 10 TEA-
533 Cl, 8 NaCl, 10 HEPES, 5 QX-314-Cl, 2 Mg-ATP, 0.3 Na-GTP and 10 EGTA, with pH 7.25, 295
534 mOsm at a holding potential of -70 mV. Picrotoxin (100μM) were added to ACSF to block IPSCs.
535 For measuring sIPSCs in the OFC excitatory neurons, recording pipettes were filled with an
536 internal solution containing (in mM) 120 CsCl, 10 TEA-Cl, 8 NaCl, 10 HEPES, 5 QX-314-Cl, 4
537 Mg-ATP, 0.3 Na-GTP and 10 EGTA, with pH 7.35, 280 mOsm holding at -70 mV. Circulating
538 ACSF were added NBQX and D-AP5 to block EPSCs. Data were acquired by Clampex 10.2
539 (Molecular Devices) and analyzed by Clampfit 10 (Molecular Devices). We confirmed the AAV
540 expression by imaging the red fluorescence of the patched cells.

541 **Wireless optogenetic activation of the OFC neurons *in vivo***

542 *Design and fabrication of flexible optoelectronic neural probes*

543 Flexible optoelectronic probes were designed using an electronic design automation
544 software (Altium Designer 18.0, Altium Limited) and produced through a conventional
545 photolithography process. Neural probes (0.1 mm-thick) were designed in a bilateral form, in
546 which the right and the left probes (0.38 mm-wide and 4 mm-long each) were separated by 2.6
547 mm, in order to access both regions of the mouse brain. Copper traces and electrodes (18 μm-
548 thick) were patterned on one side (i.e., top layer) of the polyimide substrate (25 μm-thick), while
549 the other side (i.e., bottom layer) was covered with a copper layer (18 μm-thick) to stiffen the
550 probe for penetration into brain tissue. The probe tip part, where the microscale inorganic light-
551 emitting diodes (μ-ILEDs; TR2227, Cree; blue (470 nm), 270 × 220 × 50 μm^3) were attached, was

552 not covered with a copper layer to allow light emission from both sides of the probe. The fabricated
553 probes showed the optical intensity of ~405 mW/mm^2 at the top layer and ~45.3 mW/mm^2 at the
554 bottom layer, both of which sufficiently exceeds the threshold intensity for ChR2 activation (~1
555 mW/mm^2). A 3-pin plug-n-play female pin connector (M50-3130345, Harwin) and two μ-ILEDs
556 were mounted on the top layer electrodes after applying a low-temperature solder paste
557 (SMDLTLFP10T5, Chip Quik Inc.) and soldered using a precision soldering iron (NASE-2C, JBC
558 Soldering Tools) with the temperature of 250 °C. After confirming that every component was
559 robustly attached, probes were coated with Parylene C (7 μm-thick) for waterproofing. Lastly, the
560 probes were vertically bent and attached to a 3D-printed probe holder, followed by fixing them in
561 place using epoxy (5 Minute Epoxy, Permatex).

562 *Design of programmable wireless control module with detachable configuration*

563 A Bluetooth Low Energy (BLE) based wireless control module was designed to be easily
564 attached and detached with a bilateral optoelectronic probe and a battery through plug-n-play
565 connection ((Lee *et al*, 2020; Qazi *et al*, 2019). This module controls the optical output of the μ-
566 ILEDs through smartphone manipulation. The electronic circuit of the wireless module consists of
567 a rechargeable Lithium Polymer (LiPo) battery (GM300910-PCB, PowerStream Technology; 12
568 mAh, 9 × 10 × 3 mm^3), a BLE System-on-Chip (SoC; EYSHSNZWZ, Taiyo Yuden; 8.55 × 3.25
569 × 0.3 mm^3), and various other electronic components (a linear voltage regulator, four decoupling
570 capacitors, two resistors, and two indicator LEDs). The current supplied from the LiPo battery is
571 regulated and stabilized by a voltage regulator (NCP4624DMU30TCG, onsemi) and decoupling
572 capacitors, and flows to the BLE SoC to operate the module. Two indicator LEDs (VAOL-S4RP4,
573 VCC; red (624 nm wavelength)) were placed at the output pins of BLE SoC, each connected in
574 series with a resistor (RK73H1HTTC6041F, KOA Speer; 6.04 kΩ), to visually show the current

575 operation status of the module during the animal experiment – for example, the indicator LED
576 blinks every 5 seconds during optical stimulation. The wireless control module can be
577 straightforwardly assembled with optoelectronic probes through 3-pin plug-n-play connectors
578 (male: M50-3630342, Harwin; female: M50-3130345, Harwin) and assembled with LiPo battery
579 through 2-pin connectors (male: M50-3630242, Harwin; female: M50-3130245, Harwin). Every
580 component except the LiPo battery was soldered on the flexible printed circuit board (FPCB) of
581 the wireless module ($9.3 \times 7.6 \times 0.1$ mm^3), which were designed and manufactured through the
582 same method for the μ-ILED probes. The module was wirelessly programmed over the air (OTA;
583 Nordic Device Firmware Update (DFU) bootloader) to provide a pulse (20 Hz with 25 ms pulse
584 width; i.e., 50% duty cycle) or continuous (i.e., 100% duty cycle) current to the connected bilateral
585 μ-ILED probes. The BLE-based smartphone app was developed using a commercial app
586 development software (Android Studio) and used to control the μ-ILED probes for wireless
587 optogenetics.

588 *Virus injection and probe implantation surgery*

589 We injected the AAV-CAMKIIα-eYFP (vector biolabs, VB1941) or AAV-CAMKIIα-
590 ChR2-eYFP (addgene) virus in the OFC_L (AP+2.35, ML±1.3, DV -2.5) of female WT mice
591 between P50 to P60. For the injection, we anesthetized mice using 1.5% isoflurane in oxygen
592 inhalation and performed stereotaxic surgery. Each injection contained 400nl of AAV- infused at
593 a rate of 0.4 nl/sec using a microinjector. We recovered the mice for 7 days after the injection and
594 implanted the wireless optogenetic LED probe was in the OFC.

595 *Behavior test*

596 To connect the small module part to the implanted probe on the mice head, the mice were
597 briefly anesthetized with the isoflurane inhalation. After the module was connected, the mice have

598 10 min recovery phase in their home cage. On Day0, we habituated mice wearing a module for 15
599 min in the open field chamber. On Day1, we habituated the mice wearing a module in the
600 sociability chamber for 5 min. We then presented a novel social target and a novel object for 5 min
601 and recorded their approaching behaviors to measure the sociability of the mice. On Day2, we
602 performed a sociability test with blue LED stimulation for optogenetic activation. We gave 20Hz
603 blue light stimulation by 473nm LED connected to the probe during the 5 min sociability test
604 session by using the custom-designed flexible optoelectronic neural probes. Interaction times of
605 mice were analyzed on Day1 and Day2 as described previously. On Day3, we performed an open
606 field test for 5 min with optogenetic stimulation and for 5 min without stimulation to measure the
607 effect of light activation on the locomotion behavior. After the behavior test, we performed the
608 histology of the brain samples from the mice to check the virus expression and probe implanted
609 site. We collected data only if the virus was expressed more than 65% of the total volume of the
610 OFC and the probe was targeted at the virus-expressed area.

611 **Experimental design & Statistical analysis**

612 All statistical analyses were performed using custom codes in IBM SPSS statistics 21 (IBM)
613 and OriginPro 2019(Origin,). Normal distribution of data was verified using the Shapiro-Wilk
614 normality test. For parametric tests, we used the Student's t-test to compare two groups, the one-
615 way ANOVA with Fisher's least significant difference [LSD] post hoc test to compare multiple
616 groups, and two-way ANOVA test to compare I-F curves of PV^+ neurons. For nonparametric tests,
617 we used the Wilcoxon signed-rank test to compare matched pairs, the Mann-Whitney *U* test to
618 compare between two independent groups, and the Kolmogorov–Smirnov test to compare the
619 distributions of two groups.

620

621 **Data availability**

622 This study includes no data deposition in external repositories. Further requests for data used in
623 this study can be directed to the corresponding author (shlee1@kaist.ac.kr).

624

625 **Acknowledgments**

626 We thank all members of the Lee laboratory for their helpful discussion. We also thank Dr. Soo
627 Young Kim for the discussion on the PWSI mouse model, and Emily Wheeler, Boston, for editorial
628 assistance. This work was supported by grants from the National Research Foundation of Korea
629 (2021R1A2C3012159, 2021R1A4A2001803, to S.-H.L. and 2021R1A2C4001483, to J.-W.J.) and
630 the KAIST Global Singularity Program for 2020 (to S.-H.L.). This work was also supported from
631 the Next-Generation BioGreen 21 Program (PJ016403, to S.K.) and from the Institute for Basic
632 Science (IBS-002-D1 to E.K.).

633

634 **Author contributions**

635 YSJ and DJ performed most of the experiments and contributed equally to this work; HK and EK
636 performed and evaluated patch-clamp recording experiments; JHK helped to perform *in vivo*
637 recordings and measure sniffing behavior; CYK and JWJ designed and fabricated the wireless-
638 controllable optoelectronic neural probes; YO and SGK designed and cloned the AAV-sgPV
639 vectors; YHL and CHK cloned the AAV-tdTomato vectors; SHL designed and supervised the
640 study. YSJ, DJ, SHL wrote the manuscript with the contributions from all the authors.

641

642 **Conflict of interest**

643 The authors declare that they have no conflict of interest.

644 **References**

645 Adolphs R (2003) Cognitive neuroscience of human social behaviour. *Nat Rev Neurosci* 4: 165-
646 178
647 Amodio DM, Frith CD (2006) Meeting of minds: the medial frontal cortex and social cognition.
648 *Nat Rev Neurosci* 7: 268-277
649 Beurdeley M, Spatazza J, Lee HH, Sugiyama S, Bernard C, Di Nardo AA, Hensch TK,
650 Prochiantz A (2012) Otx2 binding to perineuronal nets persistently regulates plasticity in the
651 mature visual cortex. *J Neurosci* 32: 9429-9437
652 Bicks LK, Koike H, Akbarian S, Morishita H (2015) Prefrontal Cortex and Social Cognition in
653 Mouse and Man. *Front Psychol* 6: 1805
654 Blakemore SJ (2008) The social brain in adolescence. *Nat Rev Neurosci* 9: 267-277
655 Celio MR, Blumcke I (1994) Perineuronal nets--a specialized form of extracellular matrix in the
656 adult nervous system. *Brain Res Brain Res Rev* 19: 128-145
657 Cooke BM, Chowanadisai W, Breedlove SM (2000) Post-weaning social isolation of male rats
658 reduces the volume of the medial amygdala and leads to deficits in adult sexual behavior. *Behav*
659 *Brain Res* 117: 107-113
660 Czeh B, Simon M, van der Hart MG, Schmelting B, Hesselink MB, Fuchs E (2005) Chronic
661 stress decreases the number of parvalbumin-immunoreactive interneurons in the hippocampus:
662 prevention by treatment with a substance P receptor (NK1) antagonist.
663 *Neuropsychopharmacology* 30: 67-79
664 Dityatev A, Bruckner G, Dityateva G, Grosche J, Kleene R, Schachner M (2007) Activity-
665 dependent formation and functions of chondroitin sulfate-rich extracellular matrix of
666 perineuronal nets. *Dev Neurobiol* 67: 570-588
667 Egeland B, Sroufe LA, Erickson M (1983) The developmental consequence of different patterns
668 of maltreatment. *Child Abuse Negl* 7: 459-469
669 Enwright JF, Sanapala S, Foglio A, Berry R, Fish KN, Lewis DA (2016) Reduced Labeling of
670 Parvalbumin Neurons and Perineuronal Nets in the Dorsolateral Prefrontal Cortex of Subjects
671 with Schizophrenia. *Neuropsychopharmacology* 41: 2206-2214
672 Ferguson BR, Gao WJ (2018) PV Interneurons: Critical Regulators of E/I Balance for Prefrontal
673 Cortex-Dependent Behavior and Psychiatric Disorders. *Front Neural Circuits* 12: 37
674 Filice F, Vorckel KJ, Sungur AO, Wohr M, Schwaller B (2016) Reduction in parvalbumin
675 expression not loss of the parvalbumin-expressing GABA interneuron subpopulation in genetic
676 parvalbumin and shank mouse models of autism. *Mol Brain* 9: 10
677 Fone KC, Porkess MV (2008) Behavioural and neurochemical effects of post-weaning social
678 isolation in rodents-relevance to developmental neuropsychiatric disorders. *Neurosci Biobehav*
679 *Rev* 32: 1087-1102
680 Franklin KBJ, Paxinos G *The mouse brain in stereotaxic coordinates*
681 Fuhrmann D, Knoll LJ, Blakemore SJ (2015) Adolescence as a Sensitive Period of Brain
682 Development. *Trends Cogn Sci* 19: 558-566
683 Goodwill HL, Manzano-Nieves G, LaChance P, Teramoto S, Lin S, Lopez C, Stevenson RJ,
684 Theyel BB, Moore CI, Connors BW *et al* (2018) Early Life Stress Drives Sex-Selective
685 Impairment in Reversal Learning by Affecting Parvalbumin Interneurons in Orbitofrontal Cortex
686 of Mice. *Cell Rep* 25: 2299-2307 e2294

687 Hanson JL, Chung MK, Avants BB, Shirtcliff EA, Gee JC, Davidson RJ, Pollak SD (2010) Early
688 stress is associated with alterations in the orbitofrontal cortex: a tensor-based morphometry
689 investigation of brain structure and behavioral risk. *J Neurosci* 30: 7466-7472
690 Hazan L, Zugaro M, Buzsaki G (2006) Klusters, NeuroScope, NDManager: a free software suite
691 for neurophysiological data processing and visualization. *J Neurosci Methods* 155: 207-216
692 Hensch TK (2004) Critical period regulation. *Annu Rev Neurosci* 27: 549-579
693 Hensch TK (2005) Critical period plasticity in local cortical circuits. *Nat Rev Neurosci* 6: 877-
694 888
695 Hu W, Zhang M, Czeh B, Flugge G, Zhang W (2010) Stress impairs GABAergic network
696 function in the hippocampus by activating nongenomic glucocorticoid receptors and affecting the
697 integrity of the parvalbumin-expressing neuronal network. *Neuropsychopharmacology* 35: 1693-
698 1707
699 Huang ZJ, Kirkwood A, Pizzorusso T, Porciatti V, Morales B, Bear MF, Maffei L, Tonegawa S
700 (1999) BDNF regulates the maturation of inhibition and the critical period of plasticity in mouse
701 visual cortex. *Cell* 98: 739-755
702 Kareken DA, Sabri M, Radnovich AJ, Claus E, Foresman B, Hector D, Hutchins GD (2004)
703 Olfactory system activation from sniffing: effects in piriform and orbitofrontal cortex.
704 *Neuroimage* 22: 456-465
705 Kim CY, Ku MJ, Qazi R, Nam HJ, Park JW, Nam KS, Oh S, Kang I, Jang JH, Kim WY *et al*
706 (2021) Soft subdermal implant capable of wireless battery charging and programmable controls
707 for applications in optogenetics. *Nat Commun* 12: 535
708 Kobayashi M, Hayashi Y, Fujimoto Y, Matsuoka I (2018) Decreased parvalbumin and
709 somatostatin neurons in medial prefrontal cortex in BRINP1-KO mice. *Neurosci Lett* 683: 82-88
710 Krishnan K, Lau BY, Ewall G, Huang ZJ, Shea SD (2017) MECP2 regulates cortical plasticity
711 underlying a learned behaviour in adult female mice. *Nat Commun* 8: 14077
712 Lee E, Hong J, Park YG, Chae S, Kim Y, Kim D (2015) Left brain cortical activity modulates
713 stress effects on social behavior. *Sci Rep* 5: 13342
714 Lee J, Parker KE, Kawakami C, Kim JR, Qazi R, Yea J, Zhang S, Kim CY, Bilbily J, Xiao J *et al*
715 (2020) Rapidly-customizable, scalable 3D-printed wireless optogenetic probes for versatile
716 applications in neuroscience. *Adv Funct Mater* 30
717 Lipton PA, Alvarez P, Eichenbaum H (1999) Crossmodal associative memory representations in
718 rodent orbitofrontal cortex. *Neuron* 22: 349-359
719 Lodge DJ, Behrens MM, Grace AA (2009) A loss of parvalbumin-containing interneurons is
720 associated with diminished oscillatory activity in an animal model of schizophrenia. *J Neurosci*
721 29: 2344-2354
722 Luhmann HJ, Prince DA (1991) Postnatal maturation of the GABAergic system in rat neocortex.
723 *J Neurophysiol* 65: 247-263
724 Makinodan M, Rosen KM, Ito S, Corfas G (2012) A critical period for social experience-
725 dependent oligodendrocyte maturation and myelination. *Science* 337: 1357-1360
726 Marlin BJ, Mitre M, D'Amour J A, Chao MV, Froemke RC (2015) Oxytocin enables maternal
727 behaviour by balancing cortical inhibition. *Nature* 520: 499-504
728 Matthews GA, Nieh EH, Vander Weele CM, Halbert SA, Pradhan RV, Yosafat AS, Glober GF,
729 Izadmehr EM, Thomas RE, Lacy GD *et al* (2016) Dorsal Raphe Dopamine Neurons Represent
730 the Experience of Social Isolation. *Cell* 164: 617-631

731 McCormick CM, Smith C, Mathews IZ (2008) Effects of chronic social stress in adolescence on
732 anxiety and neuroendocrine response to mild stress in male and female rats. *Behav Brain Res*
733 187: 228-238
734 McLean AC, Valenzuela N, Fai S, Bennett SA (2012) Performing vaginal lavage, crystal violet
735 staining, and vaginal cytological evaluation for mouse estrous cycle staging identification. *J Vis*
736 *Exp*: e4389
737 Mimura M, Hoeft F, Kato M, Kobayashi N, Sheau K, Piggot J, Mills D, Galaburda A, Korenberg
738 JR, Bellugi U *et al* (2010) A preliminary study of orbitofrontal activation and hypersociability in
739 Williams Syndrome. *J Neurodev Disord* 2: 93-98
740 Nakazawa K, Zsiros V, Jiang Z, Nakao K, Kolata S, Zhang S, Belforte JE (2012) GABAergic
741 interneuron origin of schizophrenia pathophysiology. *Neuropharmacology* 62: 1574-1583
742 Orduz D, Bischop DP, Schwaller B, Schiffmann SN, Gall D (2013) Parvalbumin tunes spike-
743 timing and efferent short-term plasticity in striatal fast spiking interneurons. *J Physiol* 591: 3215-
744 3232
745 Paus T, Keshavan M, Giedd JN (2008) Why do many psychiatric disorders emerge during
746 adolescence? *Nat Rev Neurosci* 9: 947-957
747 Pisu MG, Garau A, Boero G, Biggio F, Pibiri V, Dore R, Locci V, Paci E, Porcu P, Serra M
748 (2016) Sex differences in the outcome of juvenile social isolation on HPA axis function in rats.
749 *Neuroscience* 320: 172-182
750 Qazi R, Gomez AM, Castro DC, Zou Z, Sim JY, Xiong Y, Abdo J, Kim CY, Anderson A,
751 Lohner F *et al* (2019) Wireless optofluidic brain probes for chronic neuropharmacology and
752 photostimulation. *Nat Biomed Eng* 3: 655-669
753 Qazi R, Parker KE, Kim CY, Rill R, Norris MR, Chung J, Bilbily J, Kim JR, Walicki MC,
754 Gereau GB *et al* (2021) Scalable and modular wireless-network infrastructure for large-scale
755 behavioural neuroscience. *Nat Biomed Eng*
756 Radyushkin K, Hammerschmidt K, Boretius S, Varoqueaux F, El-Kordi A, Ronnenberg A,
757 Winter D, Frahm J, Fischer J, Brose N *et al* (2009) Neuroligin-3-deficient mice: model of a
758 monogenic heritable form of autism with an olfactory deficit. *Genes Brain Behav* 8: 416-425
759 Royet JP, Plailly J, Delon-Martin C, Kareken DA, Segebarth C (2003) fMRI of emotional
760 responses to odors: influence of hedonic valence and judgment, handedness, and gender.
761 *Neuroimage* 20: 713-728
762 Rudy B, Fishell G, Lee S, Hjerling-Leffler J (2011) Three groups of interneurons account for
763 nearly 100% of neocortical GABAergic neurons. *Dev Neurobiol* 71: 45-61
764 Schubert MI, Porkess MV, Dashdorj N, Fone KC, Auer DP (2009) Effects of social isolation
765 rearing on the limbic brain: a combined behavioral and magnetic resonance imaging volumetry
766 study in rats. *Neuroscience* 159: 21-30
767 Sugiyama S, Di Nardo AA, Aizawa S, Matsuo I, Volovitch M, Prochiantz A, Hensch TK (2008)
768 Experience-dependent transfer of Otx2 homeoprotein into the visual cortex activates postnatal
769 plasticity. *Cell* 134: 508-520
770 Swiech L, Heidenreich M, Banerjee A, Habib N, Li Y, Trombetta J, Sur M, Zhang F (2015) In
771 vivo interrogation of gene function in the mammalian brain using CRISPR-Cas9. *Nat Biotechnol*
772 33: 102-106
773 Ueno H, Suemitsu S, Okamoto M, Matsumoto Y, Ishihara T (2017) Parvalbumin neurons and
774 perineuronal nets in the mouse prefrontal cortex. *Neuroscience* 343: 115-127

775 Ueno H, Takao K, Suemitsu S, Murakami S, Kitamura N, Wani K, Okamoto M, Aoki S, Ishihara
776 T (2018) Age-dependent and region-specific alteration of parvalbumin neurons and perineuronal
777 nets in the mouse cerebral cortex. *Neurochem Int* 112: 59-70
778 Widom CS, DuMont K, Czaja SJ (2007) A prospective investigation of major depressive
779 disorder and comorbidity in abused and neglected children grown up. *Arch Gen Psychiatry* 64:
780 49-56
781 Wikenheiser AM, Schoenbaum G (2016) Over the river, through the woods: cognitive maps in
782 the hippocampus and orbitofrontal cortex. *Nat Rev Neurosci* 17: 513-523
783 Wohr M, Orduz D, Gregory P, Moreno H, Khan U, Vorckel KJ, Wolfer DP, Welzl H, Gall D,
784 Schiffmann SN *et al* (2015) Lack of parvalbumin in mice leads to behavioral deficits relevant to
785 all human autism core symptoms and related neural morphofunctional abnormalities. *Transl*
786 *Psychiatry* 5: e525
787

Figure Legends

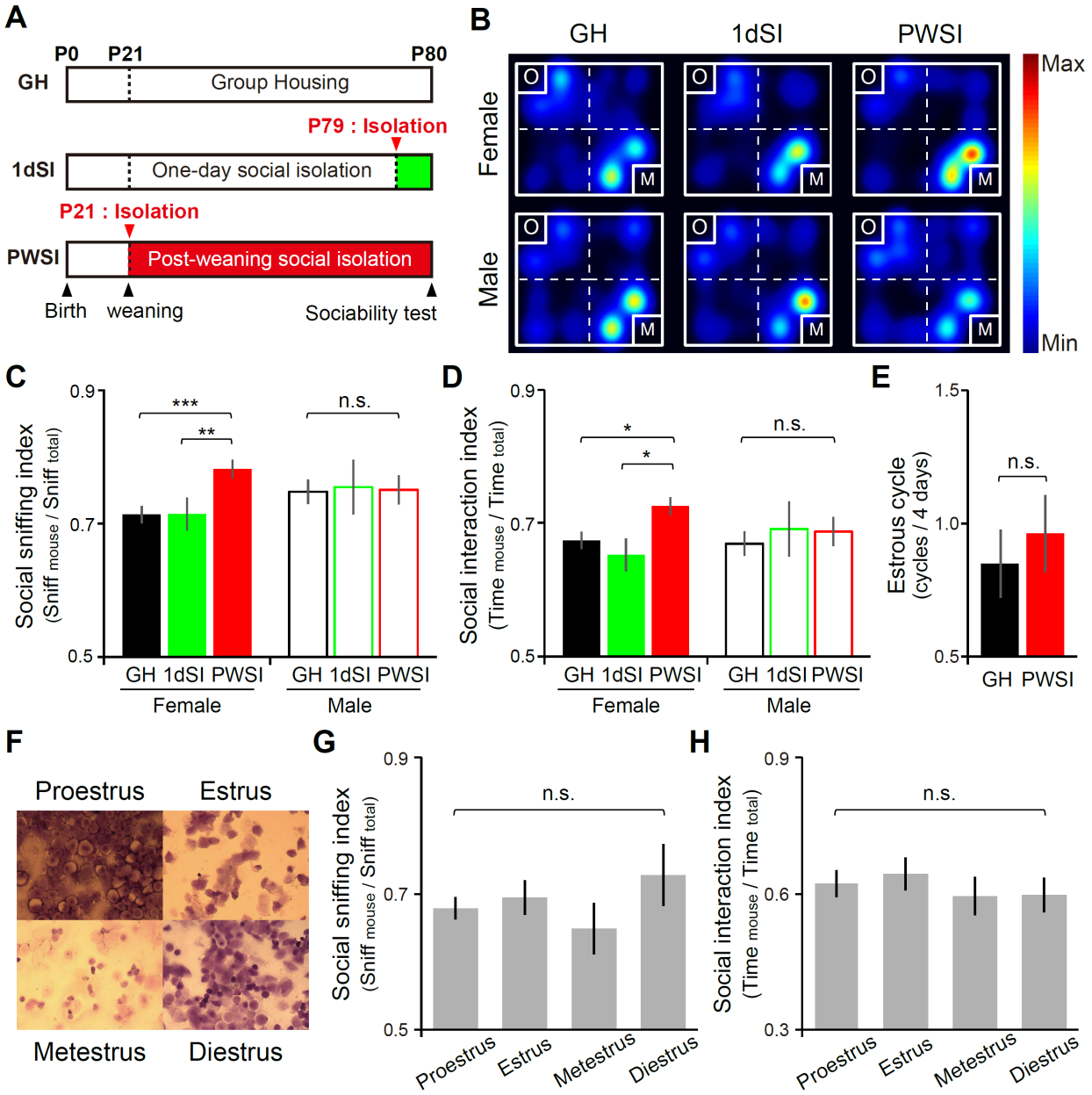

Fig 1 - PWSI during adolescence enhances social sniffing behavior in female mice.

A. Experimental design of the sociability test. Schematic of group-housing (GH), 1day social isolation (1dSI), and post-weaning social isolation (PWSI). Note that the sociability behavior was measured at P80.

794 B. Representative heat maps indicating mouse locations in the square chamber during the
795 sociability test. In the chamber, a container containing a novel object (O) and a container
796 containing the same-sex novel mouse (M) were located at diagonal corners. Heatmaps were
797 calculated in EthoVision XT as mean duration of time spent in an area for each group.
798 C. The social sniffing index displays the social sniffing times divided by the total sniffing times.
799 One-way ANOVA test, female: $F_{(2, 101)} = 8.431$, ***$P < 0.001$, male: $F_{(2, 36)} = 0.015$, $P = 0.985$,
800 Fisher's least significant difference post hoc test. Note that only the PWSI female mice showed a
801 significant increase in the social sniffing behavior.
802 D. The social interaction index displays the time spent in the social zone divided by the total time
803 spent in both object and social interaction zones. One-way ANOVA test, $F_{(2, 101)} = 3.496$, *P =
804 0.034, male: $F_{(2, 36)} = 0.109$, $P = 0.897$, Fisher's least significant difference post hoc test. Note that
805 only the PWSI female mice showed a significant increase in social interaction behavior.
806 E. The number of estrous cycles per 4 days of GH ($n = 5$) and PWSI mice ($n = 5$). The duration of
807 estrous cycles was not different between groups. Mann-Whitney U test, $P = 0.912$.
808 F. Representative images of cells in the vaginal smear that were stained with crystal violet. The
809 estrous cycles of female mice were identified based on the shape of stained cells.
810 G. The social sniffing indices of females across the estrous cycle. One-way ANOVA test, $F_{(3,30)}$ =
811 0.927, $P = 0.440$.
812 H. The social interaction indices of females across the estrous cycle. One-way ANOVA test, $F_{(3,30)}$
813 = 0.513, $P = 0.677$.
814 Data information: All data are presented as mean ± SEM. In (C-D), Female GH, $n = 54$, 1dSI, n
815 = 14, PWSI, $n = 36$; Male GH, $n = 15$, 1dSI, $n = 7$, PWSI, $n = 17$; In (G-H), Proestrus, $n = 10$,

816 Estrus, $n = 12$, Metestrus, $n = 6$, Diestrus, $n = 6$. *** $P < 0.001$, ** $P < 0.01$, * $P < 0.05$, n.s.,

817 not significant.

818

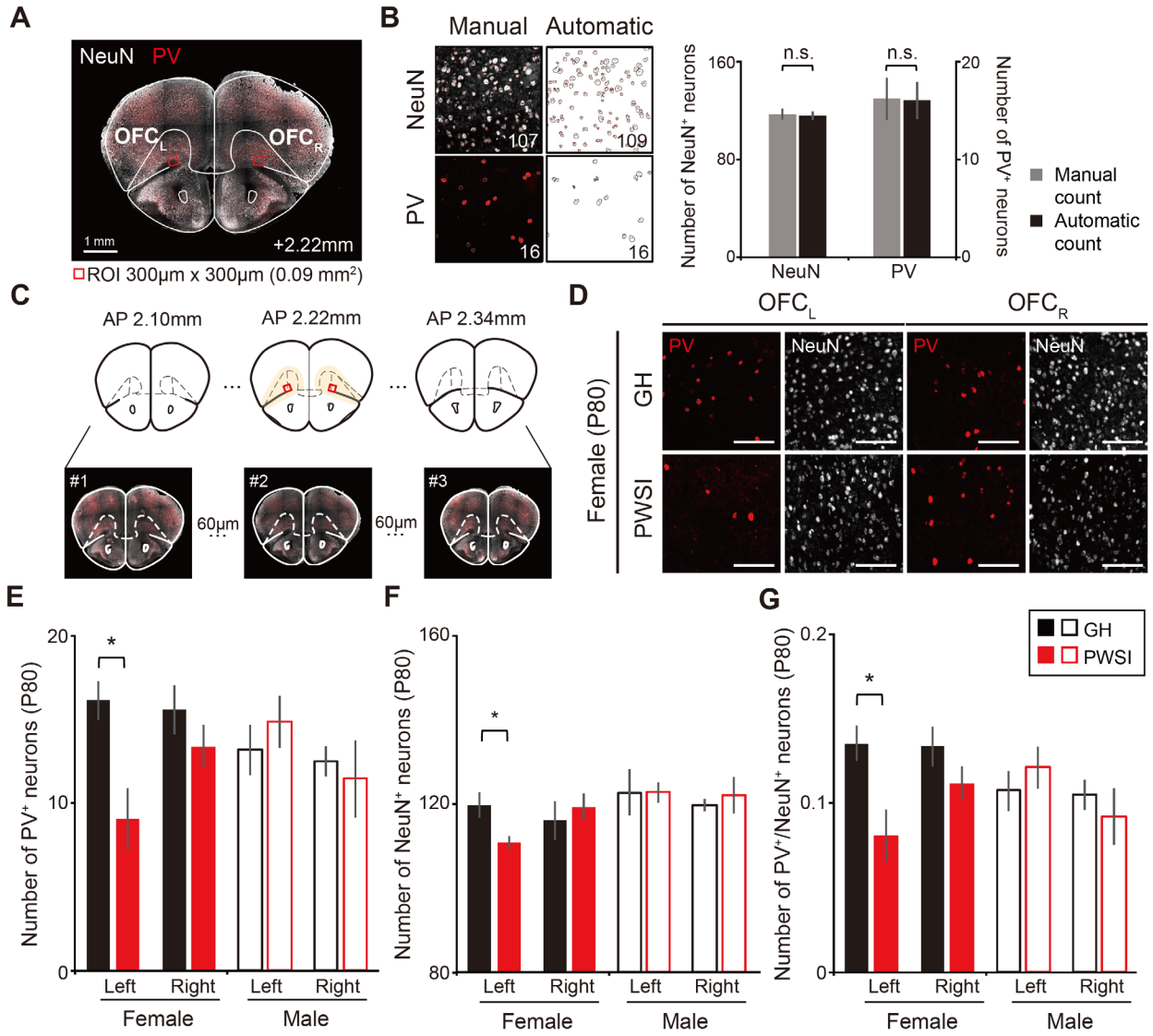

Fig 2 - PV expression in the OFC$_L$ decreases in the PWSI female mice.

A. Representative image of the immunostained PV and NeuN in the OFC of a mouse brain coronal section marked with the regions of interest (ROI, 0.09 mm^2). Scale bar, 1 mm.

B. Validation of the automatic cell counting method. Left; representative images of the PV (red) and NeuN (white) immunostained in the OFC$_L$ of GH female mice. Left panels show original images used for manual counting, and right panels show automatically detected cell boundaries from original images. Bottom numbers indicate the counted cell numbers. Bars, average numbers

828 of $NeuN^+$ and PV^+ neurons in the OFC_L of GH female mice from the manual counting (gray) and
829 automatic counting (black) (n = 6). Note that there is no difference between numbers from manual
830 and automatic counting. Mann-Whitney U test (NeuN, P = 0.200; PV, P = 1.000).
831 C. Schematic brain images showing the selection of brain slices for cell counting. Three brain
832 slices were selected between AP +2.1mm and +2.34mm with an interval of 60μm.

833 D. Representative fluorescence images of the PV (red) and the NeuN (white) immunostained in
834 the OFC_L and OFC_R of P80 GH and PWSI female mice. Scale bars, 100μm.

835 E. The number of PV^+ neurons in the OFC. PWSI decreased the number of PV^+ neurons in the
836 female OFC_L. Mann-Whitney U test (female left, *P = 0.030; female right, P = 0.297; male left,
837 P = 0.623; male right, P = 1.000).
838 F. The number of $NeuN^+$ neurons in the OFC. Mann-Whitney U test (female left, *P = 0.024,
839 female right, P = 1.000, male left, P = 0.903; male right, P =1.000).
840 G. The number of PV^+ / $NeuN^+$ neurons in the OFC. Mann-Whitney U test (female left, *P = 0.045;
841 female right, P = 0.298; male left, P = 0.540; male right, P=0.903).
842 Data information: All data are presented as mean ± SEM. In (E-G), Female, GH, n = 6 mice,
843 PWSI, n = 6 mice; Male, GH, n = 4 mice, PWSI, n = 5 mice. * $P < 0.05$.
844

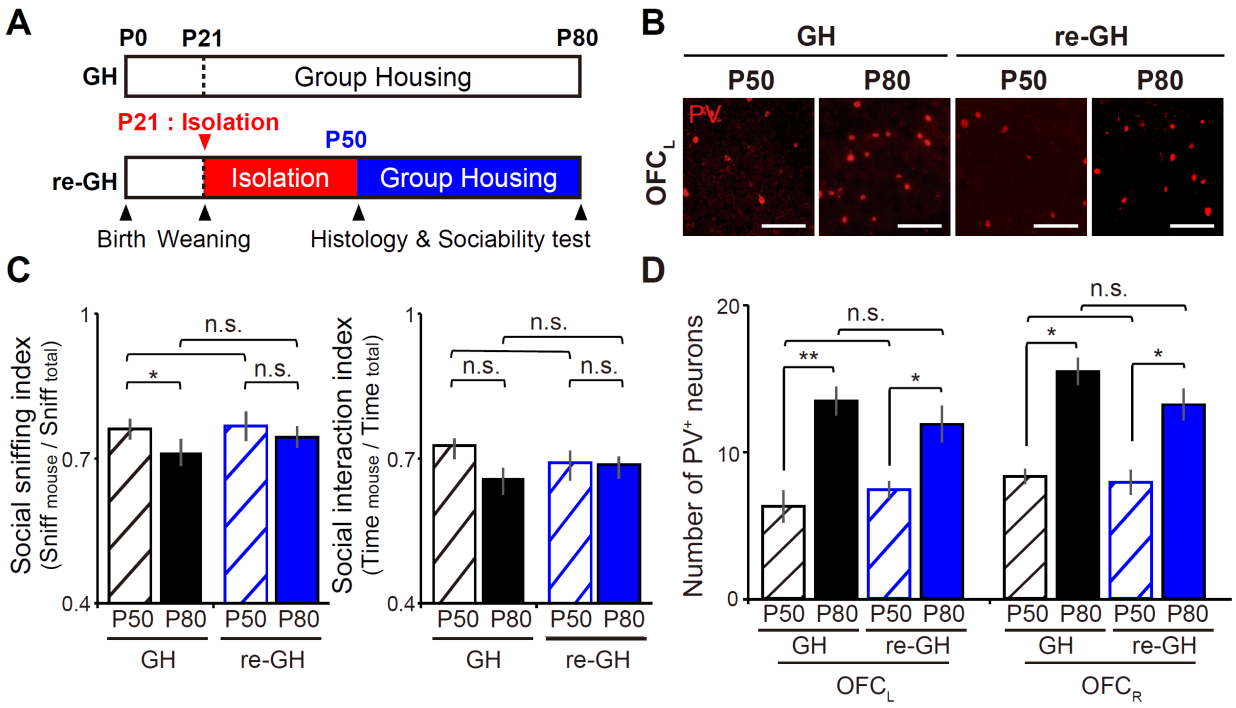

Fig 3 - Re-group-housing of PWSI female mice after P50 restores normal sociability and PV expression in the OFC$_L$.

A. Schematic illustration of group-housing (GH) or re-group-housing (re-GH) conditions. Mice were isolated at P21 and re-group-housed at P50 in re-group-housing condition. Note that the sociability test and the histology were performed at P50 and P80.

B. Representative fluorescence images of the PV immunostained in the OFC$_L$ of GH and re-GH female mice at P50 and P80. Scale bars, 100µm.

C. The results of the sociability test of the GH and the re-GH mice at P50 and P80. Left, the social sniffing index. Wilcoxon signed-rank test within group (GH, *P = 0.023; re-GH, P = 0.450) and Mann-Whitney U test between groups (P50, P = 0.555; P80, P = 0.212). Right, the social interaction index. Wilcoxon signed-rank test within group (GH, P = 0.068; re-GH, P = 0.625),

858 Mann-Whitney U test between groups (P50, $P = 0.555$; P80, $P = 0.470$). GH, $n = 11$ mice, re-GH,
859 $n = 11$ mice
860 D. The number of PV^+ neurons in the OFC. Mann-Whitney U test within group (OFC_L, GH, $^{**}P$
861 $= 0.005$; re-GH, $^{*}P = 0.030$; OFC_R, GH, $^{*}P = 0.011$; re-GH, $^{*}P = 0.014$), Mann-Whitney U test
862 between group (OFC_L, P50, $P = 0.901$; P80, $P = 0.749$; OFC_R, P50, $P = 0.934$; P80, $P = 0.285$).
863 GH, P50, $n = 11$ mice; P80, $n = 4$ mice; re-GH, P50, $n = 8$ mice, P80, $n = 6$ mice.
864 Data information: All data are presented as mean ± SEM. $^{**}P < 0.01$, $^{*}P < 0.05$, n.s., not
865 significant.
866

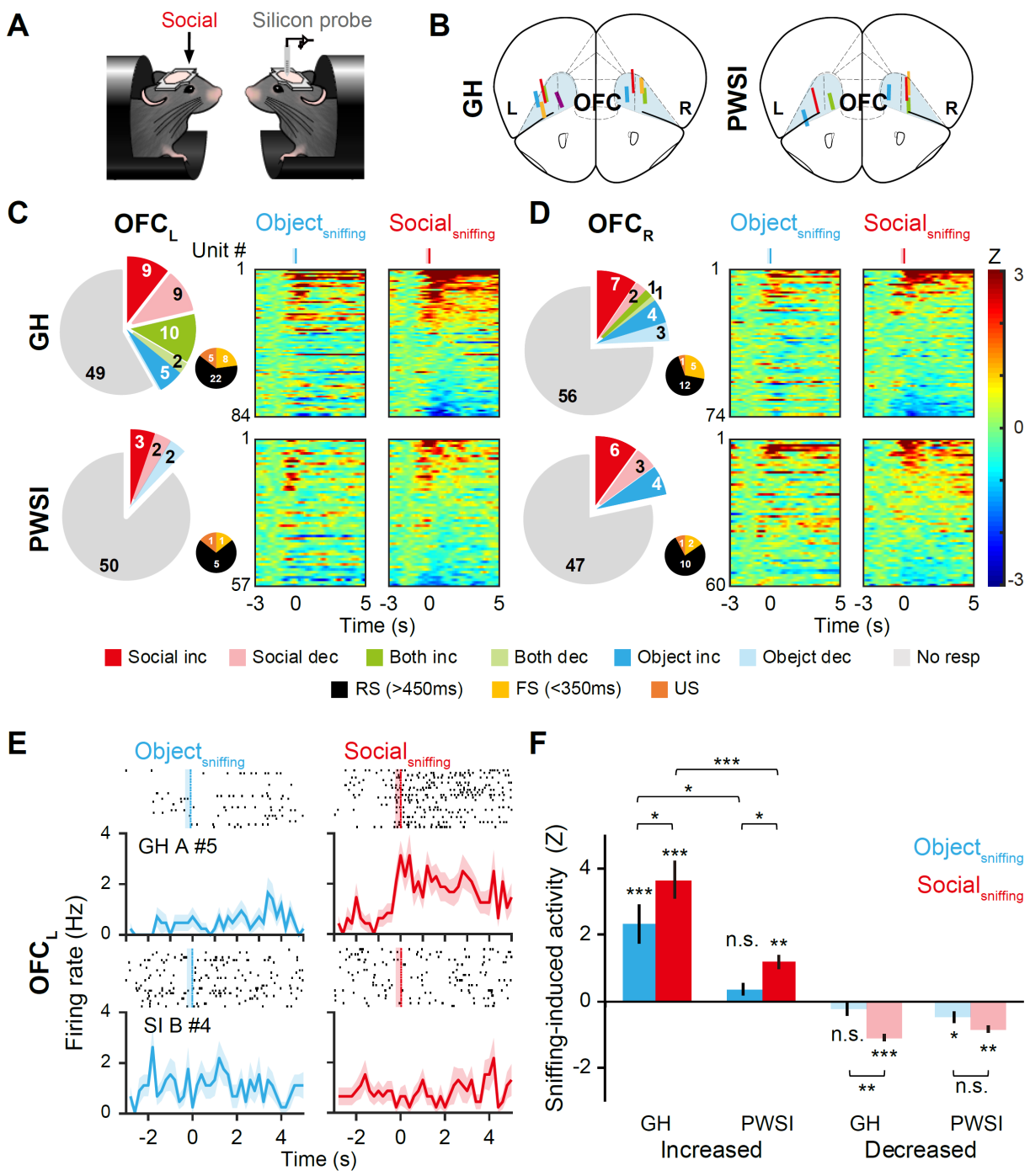

868

869 **Fig 4 - PWSI reduces sniffing-induced activity in the OFC$_L$ of female mice.**

870 A. Experimental design for *in vivo* multichannel recording of the neurons responsive to social
871 sniffing in the OFC of head-fixed mice.
872 B. Schematic illustration of mouse brain sections marked with the recording sites in the OFC of
873 GH or PWSI female mice. Blue shading, OFC; colored bars, recording sites confirmed by post hoc
874 histology.
875 C. Neural responses associated with sniffing in the female OFC_L. The large pie charts, the OFC_L
876 neurons showing social sniffing responses (Social, red), object sniffing responses (Object, blue),
877 or both social and object sniffing responses (Both, green). Inc and dec, neurons showing
878 significantly increased and decreased activities after the onset of sniffing, respectively ($P < 0.01$,
879 bootstrap); No resp., neurons that show no responses. The small pie charts, the waveforms of the
880 OFC_L neurons classified according to the waveform width. RS, regular-spiking neurons with the
881 waveform width >450ms; FS, fast-spiking neurons with the waveform width <350ms; US,
882 unclassified neurons with the waveform width between 350ms and 450ms. Heat maps, *Z*-scored
883 activity of all neurons normalized by the pre-sniffing activity. GH: $n = 5$ mice, $n = 84$ units, PWSI:
884 $n = 3$ mice, $n = 57$ units.
885 D. The same as (C) but for the OFC_R neurons. GH: $n = 4$ mice, $n = 74$ units, PWSI: $n = 4$ mice, n
886 $= 60$ units.
887 E. Representative raster plots and peri-event time histograms of example OFC_L neurons from the
888 GH female mouse (top, GH A #5) and from the PWSI female mouse (bottom, SI B #4) aligned by
889 the onset of object sniffing (left, blue) and the onset of social sniffing (right, red).
890 F. Averaged sniffing-induced activity for 2 sec (*Z* score) of the top 20% of OFC_L neurons that
891 show either increased or decreased responses after the onset of social sniffing. Bars, means ± SEM.
892 Wilcoxon signed-rank test for each bar ($Object_{sniffing}$, $Social_{sniffing}$, ***$P < 0.001$, ***$P < 0.001$ for

GH Increased; $P = 0.083$, $^{**}P = 0.004$ for PWSI Increased; $P = 0.478$, $^{***}P < 0.001$ for GH Decreased; $^{*}P = 0.045$, $^{**}P = 0.004$ for PWSI Decreased). Wilcoxon signed-rank test within a group ($\text{Object}_{\text{sniffing}}$ vs. $\text{Social}_{\text{sniffing}}$, $^{*}P = 0.047$ for GH Increased; $^{*}P = 0.023$, for PWSI Increased; $^{**}P = 0.002$ for GH Decreased; $P = 0.120$ for PWSI Decreased); Mann-Whitney U test between groups ($\text{Object}_{\text{sniffing}}$, $\text{Social}_{\text{sniffing}}$, $^{*}P = 0.019$, $^{***}P < 0.001$ for Increased activity; $P = 0.452$, $P = 0.110$ for Decreased activity). GH, $n = 17$ units, PWSI, $n = 11$ units. $^{***}P < 0.001$, $^{**}P < 0.01$, $^{*}P < 0.05$, n.s., not significant.

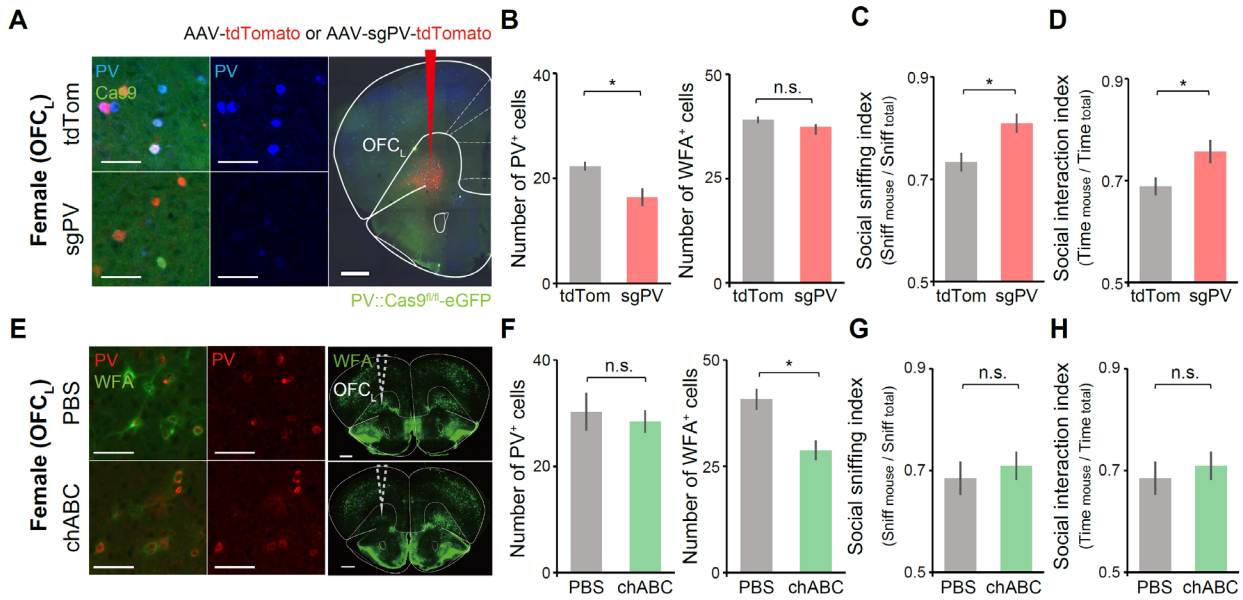

902

903 **Fig 5 – CRISPR/Cas9-mediated knock-down of PV, but not PNN degradation, in the OFC_L**

904 **enhances sociability in female mice.**

905 A. CRISPR/Cas9-mediated knock-down of PV in the female OFC_L. Left and middle,

906 representative fluorescence images of the OFC_L of the female PV::Cas9-eGFP mice injected with

907 the AAV-tdTomato (top, tdTom) or AAV-sgPV-tdTomato (bottom, sgPV). Red, tdTomato; green,

908 Cas9-eGFP; blue, immuno-stained PV. Scale bars, 50µm. Right, a representative image of the

909 OFC_L of a PV::Cas9-eGFP mouse injected with the AAV-sgPV-tdTomato. Scale bar, 1000µm.

910 B. The number of PV^+ and WFA^+ neurons in the OFC_L injected with the AAV-tdTomato (gray

911 bars) or with the AAV-sgPV-tdTomato (red bars). tdTom vs. sgPV, $n = 5$ vs. $n = 6$. Mann-Whitney

912 U test (PV^+, $*P = 0.022$; WFA^+, $P = 0.306$).

913 C. Social sniffing index of PV::Cas9 female mice injected with AAV-tdTomato (tdTom) and

914 AAV-sgPV-tdTomato (sgPV). Mann-Whitney U test, * $P = 0.021$.

915 D. Same as (C) but for social interaction index. Mann-Whitney U test, * $P = 0.034$.

916 E. chABC-induced PNN degradation in the OFC_L of female mice. Left and middle, immunostained
917 PV (red) and WFA (green) in the OFC_L of female mice injected with PBS (top) or chABC (bottom).
918 Scale bars, 50μm. Right, representative fluorescence images of the PNN stained with the WFA.
919 Note that the chABC injection selectively degraded PNNs in the OFC_L. Scale bars, 1000μm.

920 F. The number of PV^+ and WFA^+ neurons in the OFC_L injected with the PBS (gray bars) or the
921 chABC (green bars). Mann-Whitney *U* test (PV, $P = 0.609$; WFA, $*P = 0.017$), $n = 7$ for PBS, n
922 $= 7$ for chABC.

923 G. Social sniffing index of mice injected with PBS (gray) or chABC (green). Mann-Whitney *U*
924 test, $P = 0.878$
925 H. Social interaction index of mice injected with PBS (gray) or chABC (green). Mann-Whitney *U*
926 test, $P = 0.798$.
927 Data information: All data are presented as mean ± SEM. In (C-D), female PV::Cas9-eGFP mice
928 injected with AAV-tdTomato (tdTom, black and gray, OFC_L, $n = 8$ mice; OFC_R, $n = 6$ mice) or
929 with AAV-sgPV-tdTomato (sgPV, red, OFC_L, $n = 10$ mice; OFC_R, $n = 5$ mice). In (G-H), social
930 behavior in female mice injected with PBS ($n = 8$ mice) or chABC ($n = 8$ mice) into the OFC_L.
931 $*P < 0.05$, n.s., not significant.
932

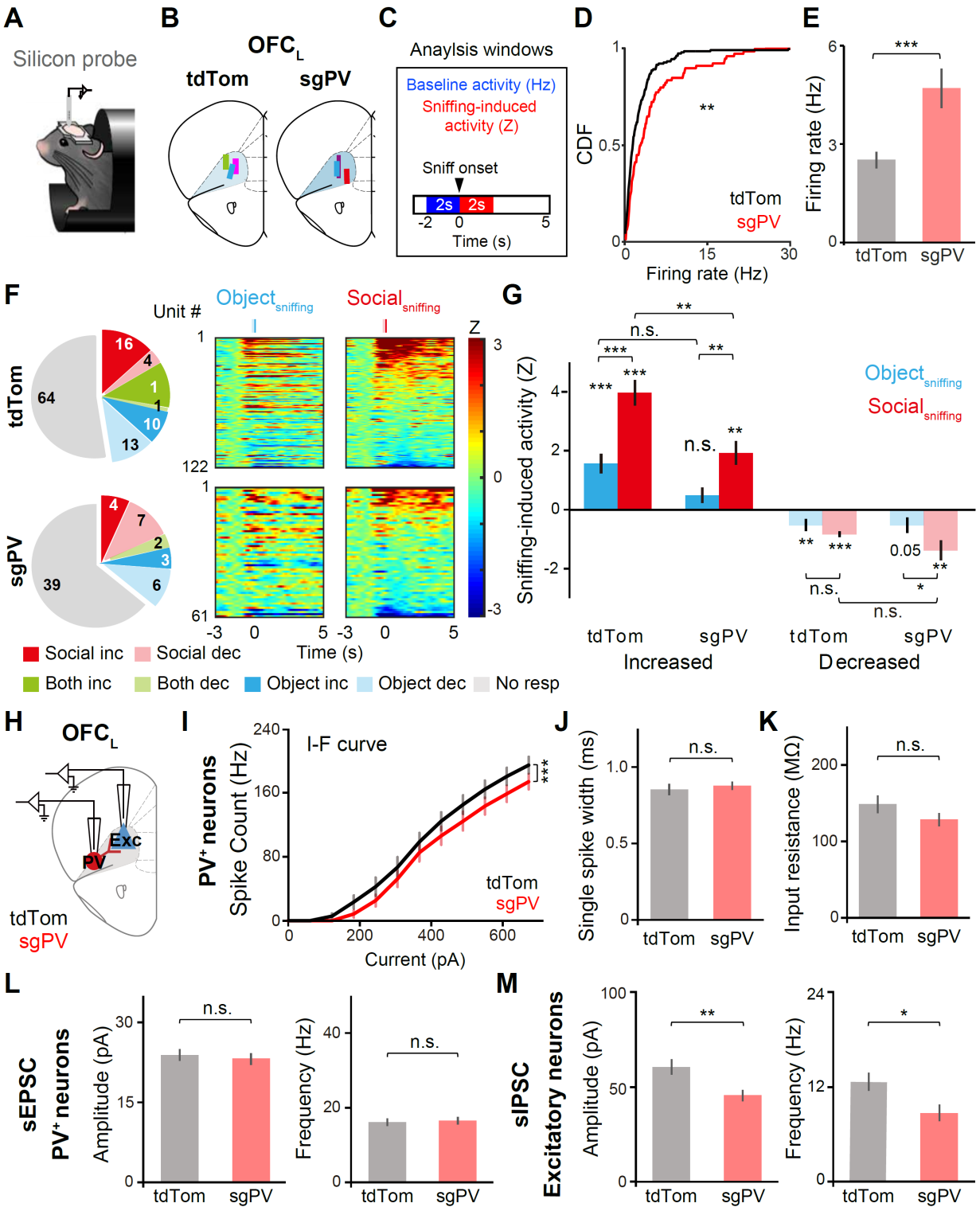

934 **Fig 6 - Knock-down of PV reduces sniffing-induced activity and decreases synaptic inhibition**

935 **in the female OFC$_L$.**

936 A. Schematic illustration of *in vivo* multichannel recording in a head-fixed mouse.

937 B. Schematic illustration of coronal brain sections of *in vivo* recording sites in the OFC_L where

938 tdTomato (tdTom)- or PV sgRNA (sgPV)-expressing AAVs were injected.

939 C. Schematic illustration of analysis windows for baseline and sniffing-induced activities of OFC_L

940 neurons. Mean firing rates during 2 sec before the sniff onset and averaged Z scores during 2 sec

941 after the sniff onset were calculated as the baseline activity and the sniffing-induced activity,

942 respectively.

943 D. The cumulative distribution function of baseline firing rates in tdTom and sgPV mice.

944 Kolmogorov–Smirnov test, $^{**}P = 0.006$.

945 E. Mean baseline firing rates of tdTom and sgPV mice. Mann-Whitney U test, $^{***}P < 0.001$.

946 F. Neural responses associated with the sniffing in the OFC_L of tdTom- (top) or sgPV-(bottom)

947 injected PV::Cas9 female mice. Pie charts, the OFC_L neurons showing social sniffing responses

948 (Social, red), object sniffing responses (Object, blue), or both social and object sniffing responses

949 (Both, green). Inc and dec, neurons showing significantly increased and decreased activities after

950 the onset of sniffing, respectively ($P < 0.01$, bootstrap); No resp, neurons that show no responses.

951 Heat maps, Z-scored activity of all recorded neurons by the pre-sniffing activity. Note that both

952 the number of sniffing-responsive neurons and social sniffing-induced activity were reduced in

953 sgPV females. Heat maps, *Z*-scored activity of all neurons normalized by the pre-sniffing activity.

954 G. Averaged sniffing-induced activity for 2 sec (*Z* score) of the top 20% of OFC_L neurons that

955 show either increased or decreased responses after the onset of social sniffing. Wilcoxon signed-

956 rank test for each bar ($Object_{sniffing}$, $Social_{sniffing}$, $^{***}P < 0.001$, $^{***}P < 0.001$ for tdTom Increased;

957 $P = 0.154$, $^{**}P = 0.006$ for sgPV Increased; $^{**}P = 0.007$, $^{***}P < 0.001$ for tdTom Decreased; P

958 $= 0.053$, $^{**}P = 0.006$ for sgPV Decreased). Note that the increased neurons showed larger activity

959 changes after social sniffing than after object sniffing. Wilcoxon signed-rank test within a group
960 ($Object_{sniffing}$ vs $Social_{sniffing}$, ***$P < 0.001$ for tdTom Increased; **$P = 0.008$ for sgPV Increased;
961 $P = 0.141$ for tdTom Decreased; *$P = 0.011$ for sgPV Decreased). Social sniffing-induced activity
962 was larger in tdTom females than in sgPV females. Mann-Whitney U test between groups
963 ($Object_{sniffing}$, $Social_{sniffing}$, $P = 0.067$, **$P = 0.004$ for Increased activity; $P = 0.720$, $P = 0.073$ for
964 Decreased activity), tdTom, $n = 24$ units, sgPV, $n = 12$ units.

965 H. Physiological properties of PV^+ neurons expressed with tdTom or sgPV. Schematic illustration
966 of the whole-cell patch-clamp recordings of PV^+ neurons (red) or excitatory neurons (blue) in the
967 PV::Cas9 mice that had been injected with the AAVs expressing either tdTom or sgPV-tdTom into
968 the OFC_L.

969 I. SgPV expression decreased the excitability of PV^+ neurons. Current-firing (I-F) curves
970 measured in the OFC_L PV^+ neurons. sgPV expression caused a significant decrease in current-
971 evoked spike counts in the PV^+ neurons. Two-way ANOVA, $F_{AAV\ (1,\ 372)} = 14.528$, ***$P < 0.001$,
972 $F_{current\ (11,\ 372)} = 121.158$, ***$P < 0.001$, $F_{AAV\ x\ current\ (11,\ 372)} = 0.388$, $P = 0.960$.
973 J. Mean half-width of spikes (ms) measured in PV^+ neurons expressed with the tdTom or the sgPV.
974 Unpaired, Student's t-test, $P = 0.628$.

975 K. Mean input resistance (MΩ) measured in PV^+ neurons expressed with the tdTom or the sgPV.

976 Unpaired, Student's t-test, $P = 0.173$.

977 L. Spontaneous EPSCs measured in PV^+ neurons of the OFC_L. Left bars, mean amplitudes (pA)
978 of sEPSCs in PV^+ neurons. Unpaired, Student's t-test ($P = 0.636$). Right bars, mean frequency
979 (Hz) of sEPSCs in PV^+ neurons. Unpaired, student's t-test ($P = 0.940$). tdTom = 10 cells (5 mice);

980 sgPV=10 cells (4 mice); female.

981 M. Spontaneous IPSCs measured in excitatory neurons of the OFC_L. Left bars, mean amplitudes
982 (pA) of sIPSCs in Pyr neurons. Unpaired, Student's t test (**P = 0.006). Right bars, mean
983 frequencies (Hz) of sIPSCs in Pyr neurons. Unpaired, Student's t test (*P = 0.015). tdTom = 16
984 cells (3 mice); sgPV=17 cells (3 mice); female.

985 Data information: All data are presented as mean ± SEM. In (D-G), tdTom: n = 6 mice, n = 122
986 units, sgPV: n = 5 mice, n = 61 units. In (I-M), tdTom = 16 cells (3 mice); sgPV = 20 cells (4 mice);
987 female. ***P < 0.001, **P < 0.01, *P < 0.05, n.s., not significant.

988

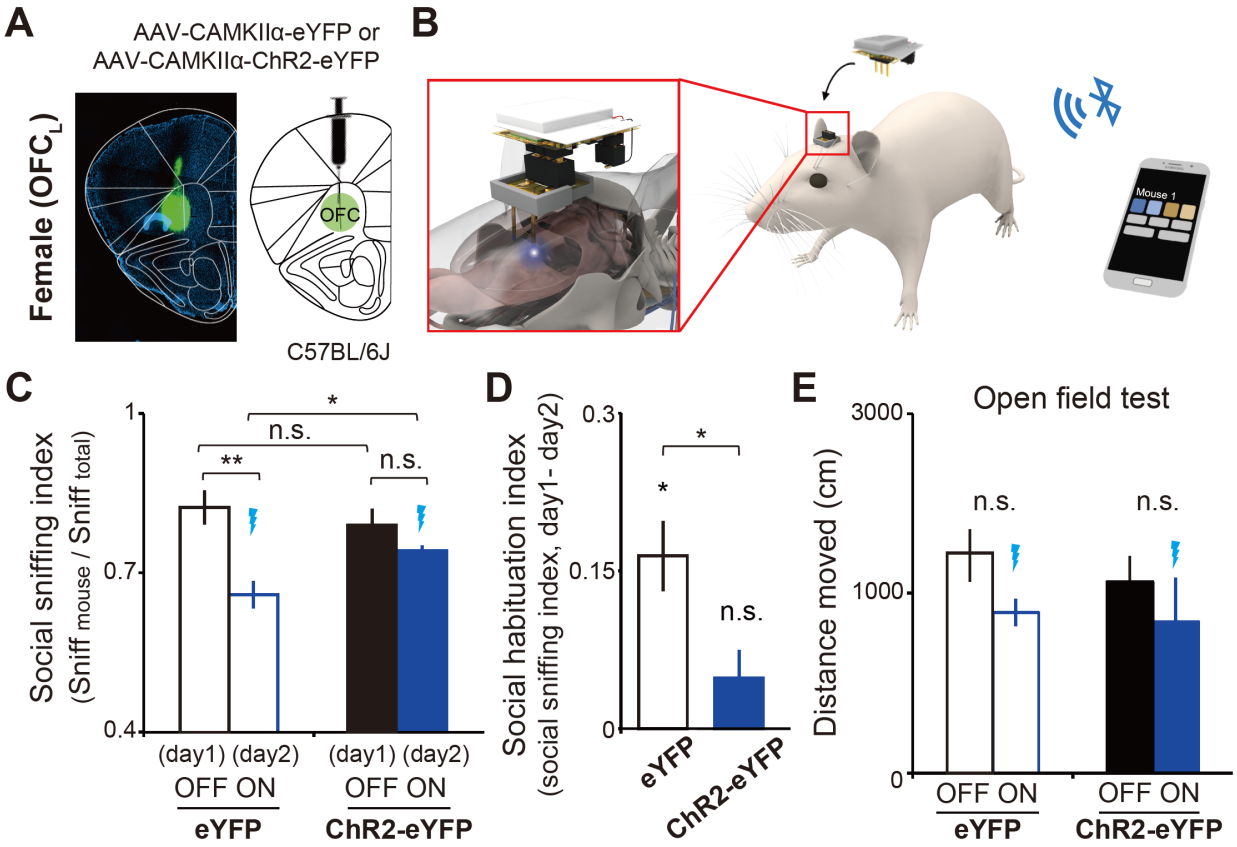

Fig 7 – Optogenetic activation of OFC$_L$ caused hypersociability in female mice.

A. Virus expression in the female OFC$_L$. Left, a representative image of the OFC$_L$ of a WT female mouse injected with the AAV-CAMKIIα-ChR2-eYFP. Green, ChR2-eYFP; blue, DAPI. Right, schematic illustration of the OFC$_L$ in the WT female mouse injected with the AAV-CAMKIIα-eYFP (eYFP) or AAV-CAMKIIα-ChR2-eYFP (ChR2-eYFP).

B. Schematic illustration of wireless optogenetic manipulation. The wireless LED probe was implanted in the OFC$_L$ of a mouse. The smartphone app modulated light on and off by Bluetooth Low Energy (BLE). 20Hz 473nm light was delivered to the OFC$_L$ during the test session.

C. The social sniffing index of eYFP (open bars) and ChR-2eYFP (closed bars) mice measured on consecutive two days. For day1, light was not delivered (OFF), and the social sniffing index was

1001 not different between eYFP and ChR2-eYFP groups. Unpaired, Student's t-test (P = 0.516). For
1002 day 2, light was delivered to the OFC_L (ON), and ChR2-eYFP group showed higher social sniffing
1003 index than eYFP group. Unpaired, Student's t-test (*P = 0.030); Paired, Student's t test within the
1004 group (eYFP, **P = 0.007; ChR2-eYFP, P = 0.179).
1005 D. Social habituation index indicates the difference in social sniffing index between day 1 (OFF)
1006 and day 2 (ON). Unpaired, Student's t-test between groups (*P = 0.036); Wilcoxon signed rank
1007 test for each group (eYFP, *P = 0.036; ChR2-eYFP, P = 0.179).
1008 E. Locomotion of mice (distance moved (cm) for 5 min) in the open field chamber was not affected
1009 by the optogenetic activation of the OFC_L. Paired, Student's t-test (OFF vs ON, eYFP, P = 0.078,
1010 ChR2-eYFP, P = 0.602). eYFP, n = 5, ChR2, n = 3; female mice.
1011 Data information: All data are presented as mean ± SEM. Blue lightning sign, delivery of light
1012 stimulation (20Hz, 473nm). In (C-D), eYFP, n = 6; ChR2-eYFP, n = 5; female mice. *P < 0.05,
1013 n.s., not significant.
1014

1015 **Suppelementary Figure Legends**

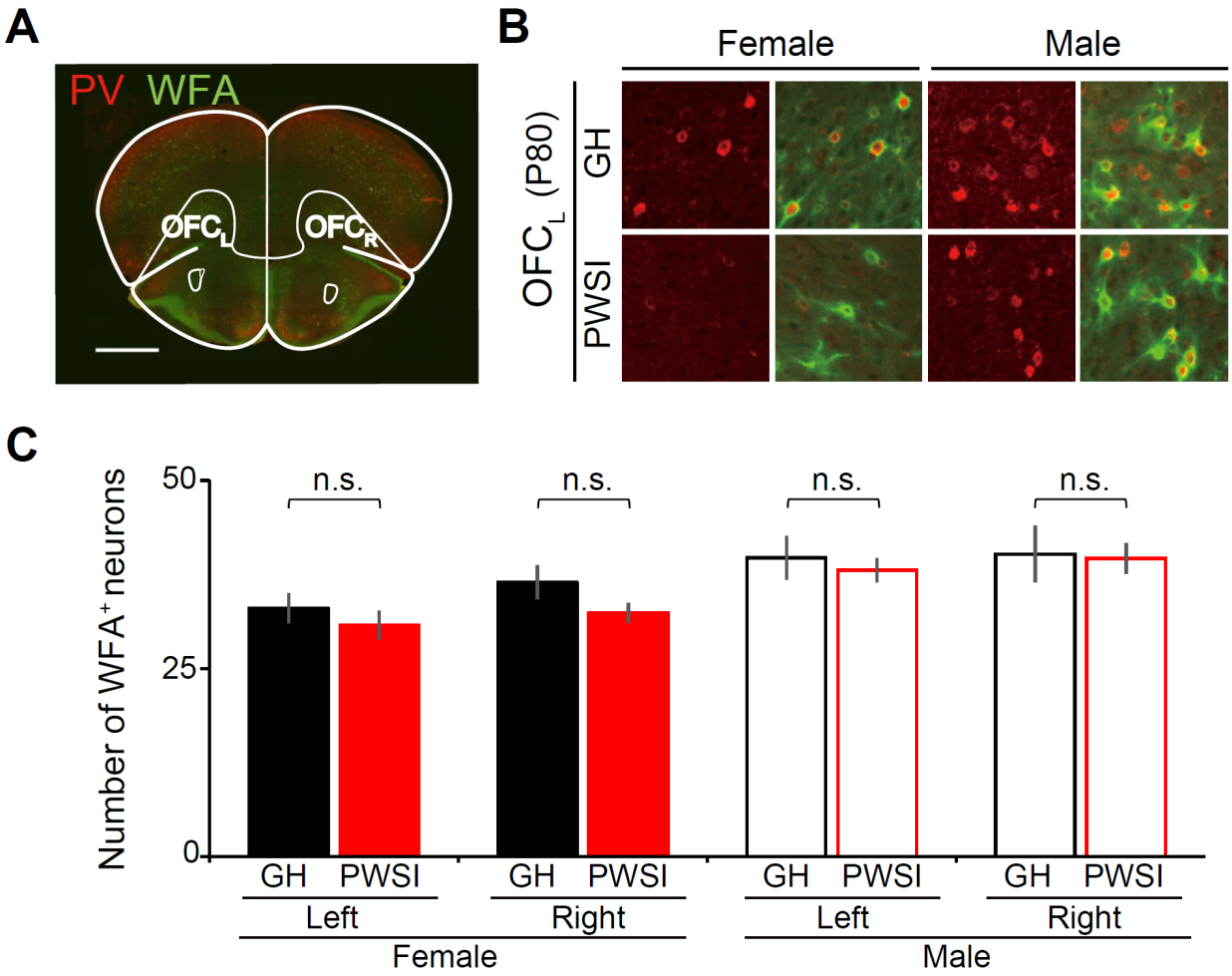

1017 **Supplementary Fig 1 – PWSI does not alter the PNN maturation in the OFC$_L$.**

1018 A. A representative image of a mouse coronal brain section that was immunostained for PV (red)

1019 and WFA (green) (scale bar, 1000μm).

1020 B. Representative fluorescence images of the OFC$_L$ immunostained with anti-PV and anti-WFA

1021 antibodies at P80 of GH and PWSI female and male mice.

1022 C. The number of WFA$^+$ neurons in the OFC left and right of male and female mice. Bars, means

1023 ± SEM. Mann-Whitney *U* test (GH vs. PWSI, female left, $P = 0.46$; female right $P = 0.185$; male

1024 left, $P = 0.337$; male right, $P = 0.442$); n.s., not significant. Females, GH, $n = 12$ mice, PWSI, n

1025 $= 11$ mice; males, GH, $n = 7$ mice, PWSI, $n = 7$ mice.

1026

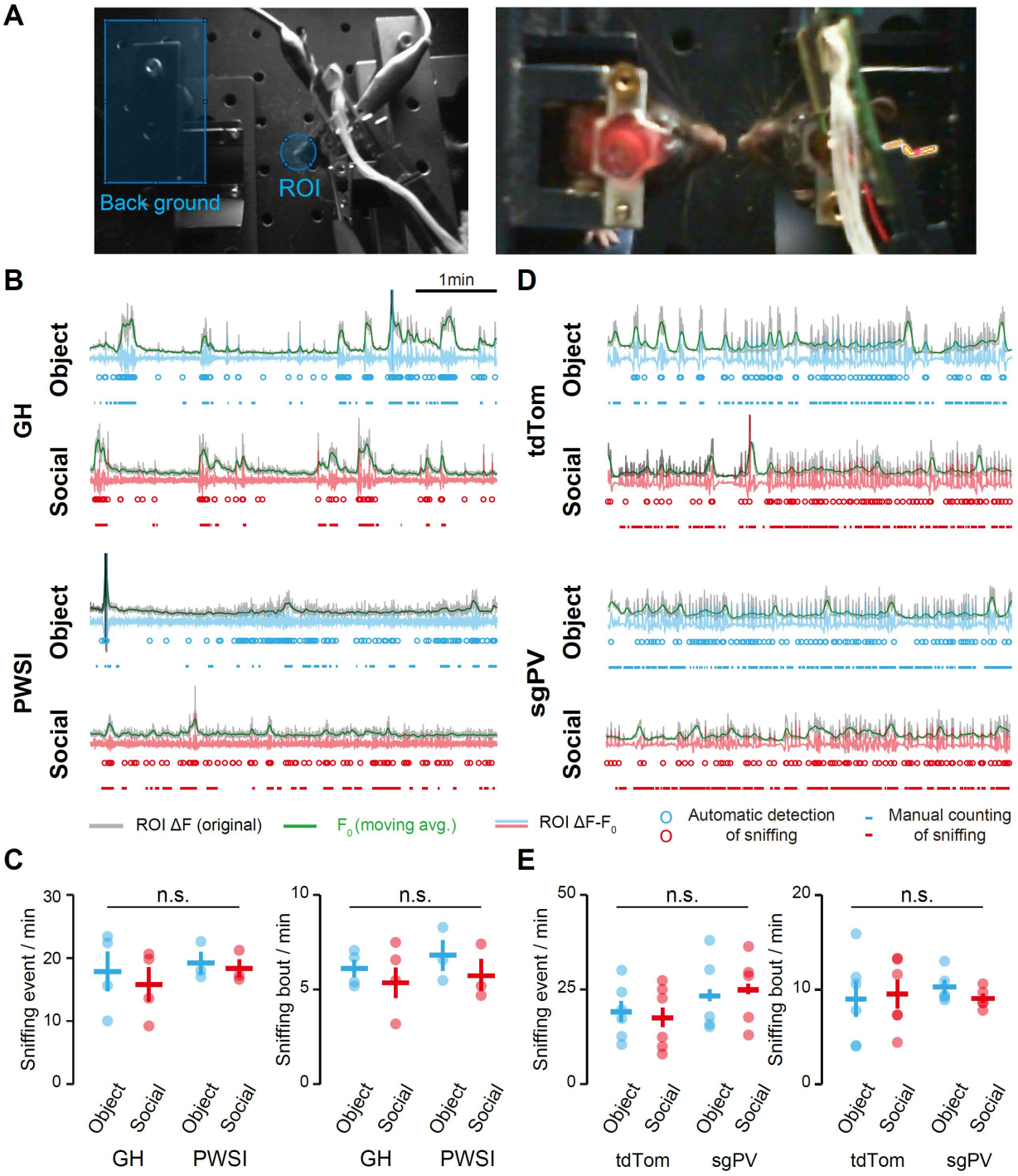

1028 **Supplementary Fig 2 - Sniffing behaviors of head-fixed mice during *in vivo* recording**

1029 A. Left, a representative image of a mouse in a movie that was analyzed for sniffing behavior. ROI,
1030 region of interest that was used for analyzing the brightness changes in the video clip. Background,
1031 an area used for normalizing the brightness changes in the ROI. Right, a zoomed-in image of head-
1032 fixed mice under the social sniffing behavior. The right mouse was a subject for *in vivo* recording.

1033 B. Representative sniffing events measured in GH or PWSI female mice. Gray trace, raw
1034 brightness changes in the ROI (ROI ΔF). Green trace, moving average in the ROI (F_0, sliding
1035 window = 50 frames). Blue and red trace, normalized brightness changes in the ROI (ROI ΔF–
1036 F_0). Circles, sniffing events were automatically detected by a Matlab-based image analysis code.
1037 Horizontal lines, sniffing events manually detected by an observer in the EthoVision XT software.
1038 Note that automatic counting methods detect sniffing events at similar times identified by manual
1039 counting. Blue, object sniffing; red, social sniffing.

1040 C. Left, sniffing events automatically counted. Dots, individual data; lines, means ± SEM.
1041 Wilcoxon signed-rank test for within a group, Object vs. Social, GH, $P = 0.465$, PWSI, $P = 1.000$.
1042 Mann-Whitney U test for between groups, GH vs. PWSI, Object, $P = 0.857$, Social, $P = 0.629$.
1043 Right, sniffing events manually identified. Dots, individual data; lines, means ± SEM. Wilcoxon
1044 signed-rank test for within a group, Object vs. Social, GH, $P = 0.686$, PWSI, $P = 0.109$. Mann-
1045 Whitney *U* test for between groups, GH vs. PWSI, Object, $P = 0.393$, Social, $P = 1.000$. GH: $n =$
1046 4 mice, PWSI: $n = 3$ mice.

1047 D. Same as (B) but for sniffing events measured in tdTom or sgPV-expressed PV::Cas9 female
1048 mice.

1049 E. Same as (C) but for tdTom and sgPV mice. Left, Wilcoxon signed-rank test for within a group,
1050 tdTom, $P = 0.463$, sgPV, $P = 0.892$. Mann-Whitney U test for between groups, Object, $P = 0.537$,
1051 Social, $P = 0.126$. Right, manual counting of sniffing bouts. Right, Wilcoxon signed-rank test for

1052 within a group, tdTom, $P = 0.528$, sgPV, $P = 0.131$. Mann-Whitney U test for between groups,

1053 Object, $P = 0.662$, Social, $P = 1.000$. tdTom: $n = 6$ mice, sgPV: $n = 5$ mice.

1054 Data information: All data are presented as mean ± SEM. n.s., not significant

1055

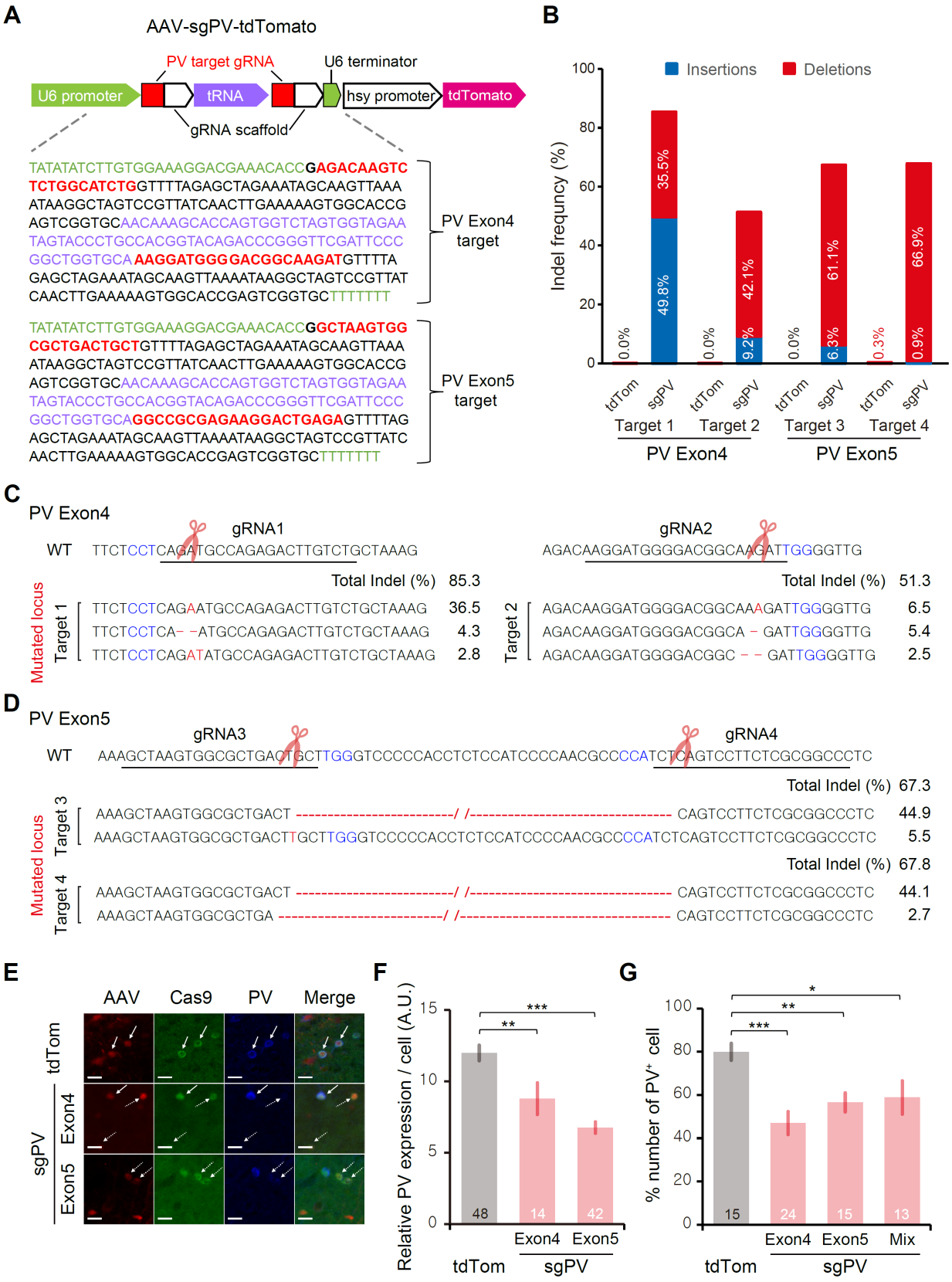
A
AAV-sgPV-tdTomato
PV target gRNA
U6 terminator
U6 promoter
tRNA
hsy promoter
tdTomato
gRNA scaffold
TATATATCTTGTGGAAAGGACGAAACACCGAGACAAGTC
TCTGGCATCTGGTTTTAGAGCTAGAAATAGCAAGTTAAA
ATAAGGCTAGTCCGTTATCAACTTGAAAAAGTGGCACCG
AGTCGGTGCAACAAAGCACCAGTGGTCTAGTGGTAGAA
TAGTACCCTGCCACGGTACAGACCCGGGTTCGATTCCC
GGCTGGTGCAAAGGATGGGGACGGCAAGATGTTTTA
GAGCTAGAAATAGCAAGTTAAAATAAGGCTAGTCCGTTAT
CAACTTGAAAAAGTGGCACCGAGTCGGTGCTTTTTTT
PV Exon4 target
TATATATCTTGTGGAAAGGACGAAACACCGGCTAAGTGG
CGCTGACTGCTGTTTTAGAGCTAGAAATAGCAAGTTAAA
ATAAGGCTAGTCCGTTATCAACTTGAAAAAGTGGCACCG
AGTCGGTGCAACAAAGCACCAGTGGTCTAGTGGTAGAA
TAGTACCCTGCCACGGTACAGACCCGGGTTCGATTCCC
GGCTGGTGCAGGCCGCGAGAAGGACTGAGAGTTTTAG
AGCTAGAAATAGCAAGTTAAAATAAGGCTAGTCCGTTATC
AACTTGAAAAAGTGGCACCGAGTCGGTGCTTTTTTT
PV Exon5 target
B
Insertions
Deletions
Indel frequncy (%)
100
80
60
40
20
0
0.0%
35.5%
49.8%
0.0%
42.1%
9.2%
0.0%
61.1%
6.3%
0.3%
66.9%
0.9%
tdTom
sgPV
Target 1
Target 2
Target 3
Target 4
PV Exon4
PV Exon5
C
PV Exon4
WT
gRNA1
TTCTCCTCAGATGCCAGAGACTTGTCTGCTAAAG
gRNA2
AGACAAGGATGGGGACGGCAAGATTGGGGTTG
Total Indel (%) 85.3
Total Indel (%) 51.3
Mutated locus
Target 1
TTCTCCTCAGAATGCCAGAGACTTGTCTGCTAAAG 36.5
TTCTCCTCA- -ATGCCAGAGACTTGTCTGCTAAAG 4.3
TTCTCCTCAGATATGCCAGAGACTTGTCTGCTAAAG 2.8
Target 2
AGACAAGGATGGGGACGGCAAAGATTGGGGTTG 6.5
AGACAAGGATGGGGACGGCA - GATTGGGGTTG 5.4
AGACAAGGATGGGGACGGC - - GATTGGGGTTG 2.5
D
PV Exon5
WT
gRNA3
AAAGCTAAGTGGCGCTGACTGCTTGGGTCCCCCACCTCTCCATCCCCAACGCCCCATCTCAGTCCTTCTCGCGGCCCTC
gRNA4
Total Indel (%) 67.3
Mutated locus
Target 3
AAAGCTAAGTGGCGCTGACT ----------/ /---------- CAGTCCTTCTCGCGGCCCTC 44.9
AAAGCTAAGTGGCGCTGACTTGCTTGGGTCCCCCACCTCTCCATCCCCAACGCCCCATCTCAGTCCTTCTCGCGGCCCTC 5.5
Total Indel (%) 67.8
Target 4
AAAGCTAAGTGGCGCTGACT ----------/ /---------- CAGTCCTTCTCGCGGCCCTC 44.1
AAAGCTAAGTGGCGCTGA ----------/ /---------- CAGTCCTTCTCGCGGCCCTC 2.7
E
AAV
Cas9
PV
Merge
tdTom
sgPV
Exon4
Exon5
F
Relative PV expression / cell (A.U.)
15
10
5
0
***
**
48
14
42
Exon4
Exon5
tdTom
sgPV
G
% number of PV+ cell
100
80
60
40
20
0
*
**
***
15
24
15
13
Exon4
Exon5
Mix
tdTom
sgPV

1057 **Supplementary Fig 3 - CRISPR/Cas9-Mediated Knock-down of PV.**

1058 A. Schematic illustration of the AAV-sgPV-tdTomato expression vector. The sgRNA vector
1059 contains the encoding sequence of tdTomato protein for the identification of transduced neurons.
1060 We used two types of AAVs to target both exon 4 and exon5 of the PV gene.
1061 B. DNA insertion (blue) and deletion (red) mutation ratio (Indel frequency) by the designed sgPVs
1062 targeting exon 4 and exon5 of the PV gene and cloned in the AAV-tdTom vector.
1063 C and D. The gRNA sequences targeting PV exon4 (C) and exon5 (D), and representative mutation
1064 patterns detected by the sequencing of the PV locus of the infected Neuro2a cells. PAM sequence
1065 indicated by blue and red scissors show CRISPR/Cas9 cutting sites. Inserted nucleotides and
1066 deleted nucleotides are indicated in red. The total indel frequency and each type of indel frequency
1067 are labeled on the right of the mutated sequences.
1068 E. Representative PV staining images of PV::Cas9 mice, which were injected with AAV-tdTomato
1069 or AAV-sgPV-tdTomato. Scale bars, 20μm. Red, tdTomato expressed by AAV vectors; green,
1070 Cas9-eGFP transgenically expressed in PV+ neurons; blue, immunostained PV proteins. Solid
1071 arrows indicate triple-positive cells, and dashed arrows indicate double-positive and PV-negative
1072 cells.
1073 F. Quantification of PV expression levels in the retrosplenial cortex (RSC), injected with AAVs
1074 that deliver tdTom or sgPVs, compared to the Cas9-eGFP expression in PV::Cas9 mice. Numbers
1075 in columns indicate the number of Cas9 positive neurons analyzed. One-way ANOVA, $F_{(2, 101)}$ =
1076 27.279, ***$P < 0.001$; Fisher's least significant difference post hoc test.
1077 G. Quantification of PV^+ cells among eGFP and tdTomato double-positive cells in the RSC
1078 injected with AAVs. Numbers in columns indicate the number of brain samples analyzed. One-
1079 way ANOVA; $F_{(3, 63)} = 6.478$, ***$P < 0.001$; Fisher's least significant difference post hoc test.

1080 **Data information:** All data are presented as mean ± SEM. ***$P < 0.001$, **$P < 0.01$, *$P < 0.05$.

1081